Scaling and labeling the high-resolution isotropic axis of two-dimensional multiple-quantum magic-angle-spinning spectra of half-integer quadrupole spins

Pascal P. Man
Systèmes Interfaciaux à l'Echelle Nanométrique, CNRS UPESA 7069, Laboratoire de Chimie des Surfaces, Université Pierre et Marie Curie, 4 Place Jussieu, Tour 55, Boîte 196, 75252 Paris Cedex 05, France
(Received 29 December 1997; revised manuscript received 9 March 1998)

The dynamics of half-integer quadrupole spins ($I=\frac{3}{2}$, $\frac{5}{2}$, $\frac{7}{2}$, and $\frac{9}{2}$) during the multiple-quantum (MQ) magic-angle spinning experiment with the two-pulse sequence, a recent NMR method, is analyzed in order to scale in frequency unit and label in ppm (the chemical shift unit) the high-resolution isotropic axis of a two-dimensional (2D) spectrum. Knowledge of the two observed chemical shifts ($\delta_{G1}^{(\mathrm{obs})}$ and $\delta_{G2}^{(\mathrm{obs})}$) of the center of gravity of an MQ-filtered central-transition peak in the two dimensions allows us to determine the true isotropic chemical shift of an absorption line, which is related to the mean bond angle in a compound. Only the isotropic chemical shift and the second-order quadrupole interaction for a sample rotating at the magic angle at a high spinning rate are considered during the free precession of the spin system. On the other hand, only the first-order quadrupole interaction for a static sample is considered during the pulses. The hypercomplex detection method is used to obtain a pure 2D absorption spectrum. The pulse program and the successive stages of data processing are described. For simplicity, only the density matrix for a spin $I=\frac{3}{2}$ at the end of the first pulse of phase φ is calculated in detail, which allows us to deduce the phase cycling of the pulse sequence that selectively detects the ± 3-quantum coherences generated by the first pulse. The positions of the echo and antiecho relative to the second pulse, and that of the MQ-filtered central-transition peak relative to the carrier frequency (ω_0) along the F_1 dimension are derived for the four half-integer quadrupole spins. The frequency offset of ω_0 relative to an external aqueous solution in the F_1 dimension is linearly related to that in the F_2 dimension. The shearing transformation, whose main interest is to shift the beginning of the acquisition period from the end of the second pulse to the echo position and to yield a high-resolution spectrum along the F_1 dimension, is presented in great detail. In the literature, two conventions are used to define the evolution period. Convention *Cz* takes the experimental evolution period as the evolution period, whereas convention *Ck* considers the echo position relative to the first pulse as the evolution period. The true isotropic chemical shift, the second-order quadrupole shift of the center of gravity of a peak, and the parameter $C_{Q\eta}$ relating the quadrupole coupling constant with the asymmetry parameter are functions of $\delta_{G1}^{(\mathrm{obs})}$ and $\delta_{G2}^{(\mathrm{obs})}$; their relationships depend on the conventions. In fact, convention *Ck* introduces a scaling factor (depending on the spin and the coherence order) that modifies not only the spectral width and the linewidth, but also the positions of the spinning sidebands in the F_1 dimension. Convention *Cz* is recommended for linewidth comparison. The analytical expressions are checked using ^{87}Rb ($I=\frac{3}{2}$) in the extensively studied $RbNO_3$ powder with two carrier frequencies: 98.2 and 163.6 MHz. Our data are in agreement with those of the literature. [S0163-1829(98)01429-5]

I. INTRODUCTION

Two-dimensional (2D) high-resolution NMR applied to spin $I=\frac{1}{2}$ systems[1–4] has given new insights into molecular structure. Similar development on spin $I=\frac{1}{2}$ systems in solids has occured.[5] Most of the elements in the Periodic Table are quadrupole nuclei with spin I larger than $\frac{1}{2}$, which are sensitive to the electric-field gradient (EFG) generated by their surroundings. The present paper deals with NMR experiments in which the interaction of the spin system with the strong static magnetic field $\mathbf{B}_0$ is much larger than the quadrupole interaction. In this condition, we are used to taking into account the first two expansion terms of this interaction, namely, the first- and second-order quadrupole interactions.[6–14] Single-quantum (SQ) transitions between consecutive energy levels as well as multiple-quantum (MQ) transitions between nonconsecutive energy levels occur during the excitation of the spin system by a radiofrequency (rf) pulse. Most of the methods discussed in this paper deal with the second-order quadrupole interaction, which is inversely proportional to $\mathbf{B}_0$ and which has the property of *shifting an absorption line* from its true isotropic chemical shift $\delta_{\mathrm{CS}}^{(\mathrm{iso})}$ to the observed chemical shift of its center of gravity $\delta_{G2}^{(\mathrm{obs})}$. For half-integer quadrupole spins ($I=\frac{3}{2}$, $\frac{5}{2}$, $\frac{7}{2}$, and $\frac{9}{2}$), usually only one-dimensional (1D) absorption lines or 2D peaks of the central transition are observed.

The first 2D method on half-integer quadrupole spins in solids is the nutation.[15–21] The experiment consists in acquiring a series of free-induction decays (FID) following a single rf excitation pulse for increasing pulse durations. The F_1 dimension of the 2D spectrum is the axis of the nutation frequencies of the spin system around the rf magnetic field $\mathbf{B}_1$. The implementation is simple, but the interpretation is not obvious because *the 2D spectrum associated with a single crystallographic site may consist of several peaks along the F_1 dimension*; these peaks are related to the nutation frequencies. Furthermore, only the SQ coherences gen-

erated by the rf pulse are detected by the rf coil; the MQ coherences are not. Rotary-echo[22,23] and off-resonance nutations[24,25] have also been introduced. Extensive computer simulation of experimental spectra is necessary to extract the two quadrupole parameters: the quadrupole coupling constant e^2qQ/h and the asymmetry parameter η. Haase and co-workers[26,27] explored a two-pulse FID method that yields the inner-satellite powder spectrum directly, providing the two quadrupole parameters independently. However, axial peaks may distort the spectrum. Meanwhile Spiess's group[5] has developed 2D exchange spectra on the spin $I=1$ system, giving dynamic information. More recently has appeared dynamic-angle spinning (DAS) methodology[28] which provides 2D SQ/SQ correlation spectra where *the 2D spectrum associated with a single site is characterized by a single peak*. A shearing transformation of the data is necessary during the processing to yield a high-resolution isotropic spectrum for the F_1 dimension. The spectrum becomes a 2D isotropic/anisotropic correlation spectrum. Switching-angle spinning (SAS) is also based on the 2D technique.[29] The simulation of its rather complex 2D contour plot provides the relative orientation of the chemical shift tensor with respect to the EFG tensor. Both DAS and SAS require a specialized probehead with a rotor and apply three rf pulses. For SAS, the spinning axis of the rotor with respect to $\mathbf{B}_0$ is at an arbitrary angle during the evolution period, defined by the duration between the first two rf pulses, and at the magic angle during the acquisition period, which starts at the end of the last rf pulse. DAS uses a specific pair of complementary angles of the rotor spinning axis in these two periods. SAS acquires the FID following the last rf pulse, whereas DAS records the echo signal. Both methods take into account the central transition only, and thus consider the spin system as a two-energy level system. Three-dimensional dynamic-angle correlation spectroscopy (DACSY) has been developed.[30]

Recently Frydman's group[31,32] introduced the multiple-quantum magic-angle spinning (MQ-MAS) methodology. In MQ spectroscopy, the rf pulses with a carrier frequency ω_0 excite nuclear-spin coherences with oscillation frequencies that are nearly multiples of ω_0. The oscillation of these coherences is then detected indirectly through its effect on the SQ absorption lines near ω_0.[33] This spectroscopy is based on 2D methods. The MQ-MAS methodology takes advantage of the properties of the MQ coherences to generate high-resolution isotropic spectra along the F_1 dimension (see Sec. II D), giving the number of different crystallographic sites in a compound when conventional 1D MAS experiment provides overlapping absorption lines. Among all the coherences generated by the first rf pulse, the specific MQ coherences are detected selectively[34] by phase cycling the rf pulses and the receiver in a two-pulse spin-echo sequence. The rotor spinning axis is at the magic angle throughout the experiment. Thus a standard MAS probehead suffices for the experiment, but the NMR spectrometer must be equipped with a digital dephaser of the rf pulses. The interactions considered between the two rf pulses and during the acquisition period define the nature and position of the echoes, whereas the interactions considered during the rf pulses affect the amplitude of the echoes. On the other hand, the shape and spectrum of the echoes observed in a powder are affected by the two pulse durations more than the interactions acting during the rf pulses do.[12,35,36] The optimum experimental conditions for the MQ-MAS experiments are: strong rf pulses, small offset, and high rotor spinning rate.[32,37] Quantitative results on spin populations are not obvious[12] but possible in particular conditions.[32,37] A 2D MQ-MAS spectrum represents the correlation of a specific MQ coherence in the F_1 dimension with a SQ coherence in the F_2 dimension. *The 2D spectrum associated with a single site consists of a single peak*—an MQ-filtered central-transition peak (simply called the peak in the remainder of the paper)—but tilted. A shearing transformation, carried out on the experimental data before the Fourier transformation versus the evolution period, yields a powder spectrum along the F_2 dimension and a high-resolution, featureless line shape in the F_1 dimension. The sheared 2D spectrum becomes a 2D isotropic/anisotropic correlation spectrum. It appears that MQ-MAS gives the same results as DAS but with a standard MAS probehead, opening new fields of investigation that DAS cannot explore, for example, nuclei with short spin-lattice relaxation times or variable temperature experiments. In fact, these two methodologies are complementary.[38] The spinning sidebands in the F_1 dimension, if present, arise from modulations of first-order quadrupole effects.[39]

Thereafter, MQ-MAS leads to numerous developments, which are focused on the production of a pure 2D absorption spectrum by designing various coherence transfer pathways,[40,41] including the z-filter sequence;[41–46] the effects of the rotor spinning rate and the excitation conditions on the spectra;[47] the optimization of the experimental conditions;[37,45] the synchronization of data acquisition with rotor spinning, which produces better sensitivity and improves line shape.[44–46] Vosegaard *et al.*[48] proposed the MQ quadrupole Carr-Purcell-Meiboom-Gill MAS experiment which improves the sensitivity of the MQ-MAS spectrum by splitting the second-order powder line shape in the F_2 dimension into manifolds of spin-echo ''sidebands'' while preserving high resolution in the F_1 dimension. For moderate values of e^2qQ/h (smaller than 4 MHz), the method, called rotation-induced adiabatic coherence transfer, is insensitive to the magnitude of e^2qQ/h and, therefore, it provides quantitative results on spin populations.[49] Structural data via homonuclear $H_{D(II)}$ and heteronuclear $H_{D(IS)}$ magnetic dipole interactions are also provided by MQ-MAS methodologies.[50] Brown and co-workers[42,43,51] avoid the shearing transformation, which distorts line shapes in the final 2D spectrum, by developing novel amplitude- and phase-modulated ''split-t_1'' MQ-MAS experiments.

Extensions of the MQ approach to well established methods have also appeared such as variable-angle spinning[38] (MQ-VAS) that can provide chemical shift anisotropy data, the double rotor (MQ-DOR),[52] shaped-pulse excitation that produces better sensitivity,[53] high-power decoupling,[54,55] cross-polarization,[56–58] or heteronuclear correlation by observing a spin-$\frac{1}{2}$ nuclei coupled to a half-integer quadrupole spin producing better resolution.[58] Experimental verification and application of the above-mentioned methods have already been carried out on the four half-integer quadrupole spins: spin-$\frac{3}{2}$ such as boron-11,[59] rubidium-87,[38,41,45,51,60] or sodium-23;[31,32,37–39,42,43,45,47–50,53–55,61–64] spin-$\frac{5}{2}$ such as manganese-55,[31,37,52] aluminum-27,[25,31,38,40,41,44,46,51,52,56,61,62,65–71] or

oxygen-17;[38,55,72,73] spin-$\frac{7}{2}$ such as cobalt-59 (Ref. 37) or scandium-45,[38] and spin-$\frac{9}{2}$ such as niobium-93.[37] The two most studied nuclei are sodium-23 and aluminum-27.

Conventional 1D MAS spectra obtained with short rf pulse duration allow the determination of the spin populations if the absorption lines are not overlapping. If not, we can use the MQ-MAS methodology to determine the number of peaks or crystallographic sites, their true isotropic chemical shifts, and the quadrupole parameters. Thanks to these data, we can simulate the 1D MAS spectra to obtain the spin population of each site.[59]

Provided that the 2D MQ-MAS spectrum is labeled in chemical shift unit and the zero ppm positions in both axes are defined, knowledge of the two observed chemical shifts of the center of gravity $\delta_{G1}^{(\mathrm{obs})}$ and $\delta_{G2}^{(\mathrm{obs})}$ of a peak in the two dimensions of a sheared MQ-MAS spectrum enables us to determine the true isotropic chemical shift of an absorption line,[32,41,45] which is related to the mean-bond angle in a compound.[40,74] Labeling of unsheared spectra[25] is extensively used by Amoureux and co-workers.[65–72] The observed chemical shift of the center of gravity of a peak along the F_2 dimension, $\delta_{G2}^{(\mathrm{obs})}$, is obtained experimentally by using an external aqueous solution. There is little work on the labeling of the high-resolution isotropic axis of the F_1 dimension,[32,41,45] because this operation requires the analytical expression of the offset Ω_{F_1}, in the F_1 dimension, of ω_0 relative to the external aqueous solution [see Eqs. (74) and (75)]. This offset depends on the definition of the evolution period that changes the spectral width in the F_1 dimension. This is why this axis is either unlabeled[42,43,51] or labeled with poorly defined conditions.[25,62,63]

The present paper is devoted to scaling and labeling the high-resolution isotropic axis of sheared 2D MQ-MAS spectra consisting in *MQ-filtered central-transition peaks*. It is a sequel to an earlier one dealing with the effects of the second-order quadrupole effects on the Hahn echoes in fast rotating solids at the magic angle.[12] Here, the analytical expressions, resulting from calculations about the echo and antiecho signals in the two-pulse MQ-MAS experiment, are for single crystals but in practice their applications are also valid for powder samples. We focus on the simplest case of the 3Q-MAS spectrum obtained with the two-pulse sequence applied to a spin $I=\frac{3}{2}$ system, which is the easiest system. Our presentation on 3Q-MAS of a spin $I=\frac{3}{2}$ differs slightly from that of Massiot *et al.*,[41] who dealt with the 3Q-MAS of a spin $I=\frac{5}{2}$ system. Results on the other three half-integer quadrupole spins are only given as a generalization. Up to Sec. II D, we shall use our own notations for the four time-domain parameters: t_1 and t_3 are the first- and second-pulse durations, τ_2 is the experimental or MQ coherence evolution period, and τ_4 the acquisition period (see Fig. 1). From Sec. II E, standard notations are used: t_1 is the experimental or MQ coherence evolution period, and t_2 is the acquisition period.

Section II A summarizes our previous calculations on the density operator describing the spin system from the thermodynamic equilibrium to the end of an x pulse.[12] A density-matrix element is referred to by two half-integer magnetic numbers r and c for row and column [see Eq. (7)]. Since a strong rf pulse with a short pulse duration is applied, the rotor appears to be static during the rf pulse. In other words, the spin system can be described by time-independent interactions. The main interaction that the spin system is submitted to is the first-order quadrupole interaction for a static sample. Therefore the quadrupole coupling ω_Q,[12] which depends on the orientation of the crystal with respect to $\mathbf{B}_0$, affects the amplitude of the FID following the rf pulse. For a powdered sample, a computer is needed to average the response of the spin system over all the orientations of the crystal with respect to $\mathbf{B}_0$ in order to predict the experimental amplitude of the FID. Section II B describes the density matrix associated with an rf pulse dephased by an angle φ_1 relative to an x pulse, which is an important ingredient of the MQ-MAS methodology. The selective detection of an MQ coherence, performed by phase cycling the rf pulses and the receiver, is shown in Sec. II C. Section II D derives the positions of the echo and antiecho in the time domain as well as those of the associated peaks in the F_1 dimension of a 2D spectrum.[12,13,36,42,43] The echo and antiecho pathways are also defined for the four half-integer quadrupole spins. The phase of the two rf pulses and that of the receiver, written for the hypercomplex or States *et al.* method[41,75–77] for generating quadrature detection in the t_1 domain, are presented in Table II. This method yields pure 2D absorption spectra. The

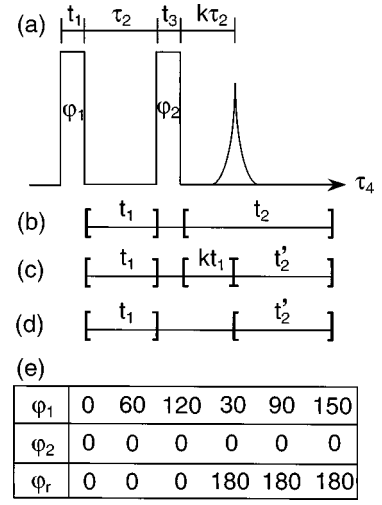

φ_1	0	60	120	30	90	150
φ_2	0	0	0	0	0	0
φ_r	0	0	0	180	180	180

FIG. 1. Various meanings of the time-domain parameters. (a) Our own notations: t_1 is the first-pulse duration, τ_2 is the experimental or MQ coherence evolution period, t_3 is the second-pulse duration, and τ_4 is the acquisition period beginning at the end of the second rf pulse; the position of the echo involved in the MQ-MAS methodology is $\tau_4=k(I,p)\tau_2$. (b) Standard notations used in the two-pulse MQ-MAS experiment: t_1 is the experimental evolution period and t_2 is the experimental acquisition period. (c) Notations involved in convention *Ck* used by Massiot *et al.* (Ref. 41) and Wang *et al.* (Ref. 38), $(1+k)t_1$ is the evolution period and t_2' is the shifted-acquisition period after the shearing transformation. (d) Notations involved in convention *Cz* used by Medek *et al.* (Ref. 32) and Hanaya and Harris (Ref. 45): t_1 is the MQ evolution period and t_2' is the shifted-acquisition period after the shearing transformation. (e) The six-step phase cycling (Ref. 34) of the two-pulse 3Q-MAS sequence for any half-integer quadrupole spin: φ_1 and φ_2 are the phase of the first and second rf pulses, respectively, and φ_r is the receiver phase. The acquisition methods (hypercomplex or TPPI) for generating quadrature detection in the t_1 domain and pure 2D absorption peak are not considered.

procedure for processing the experimental data is also given. Section II E explains why a 2D MQ-MAS spectrum is tilted and presents the shearing transformation, which changes the 2D MQ/SQ correlation spectrum to a 2D isotropic/anisotropic correlation spectrum whose F_1 dimension becomes a high-resolution isotropic axis.[32,41,76] The spectral width SW1 in the F_1 dimension of a 2D MQ-MAS spectrum is equal to the inverse of the increment of the evolution period. Unfortunately, two definitions of the evolution period appear in the literature, giving two conventions for *scaling in frequency units the spectral width SW1 of the high-resolution isotropic axis*. The first convention[32,45] (Cz) considers the experimental evolution period as the evolution period; therefore $SW1_{Cz}=1/\Delta t_1$, Δt_1 being the increment of the experimental evolution period. The second convention[38,41] (Ck) considers the position of the echo relative to the first rf pulse, equal to $(1+k)$ times the experimental evolution period, as the evolution period; therefore $SW1_{Ck}=1/[(1+k)\Delta t_1]$. The scaling factor $(1+k)$ in the evolution period of convention Ck affects the spectral width $SW1_{Ck}$. In contrast, convention Cz does not introduce a scaling factor. In Sec. II F, the expressions of the true isotropic chemical shift of a peak, those of the offset of the carrier frequency in the F_1 dimension relative to an aqueous solution, those of the second-order quadrupole shift of the center of gravity of a peak, and the parameter $C_{Q\eta}=(e^2qQ/h)(\eta^2/3+1)^{1/2}$ relating the quadrupole coupling constant to the asymmetry parameter are deduced for the two conventions. The parameter $C_{Q\eta}$ is of particular importance for characterizing materials that have featureless NMR line shapes in the F_2 dimension, such as glasses,[40] where the asymmetry parameter η cannot be deduced by line-shape analysis. All the above-mentioned parameters allow us to describe the two procedures, associated with conventions Cz and Ck, for *labeling the spectral width of the F_1 dimension in chemical shift unit (ppm) and defining the zero ppm position* of the external aqueous solution.

Section III provides experimental details. The spin $I=\frac{3}{2}$ rubidium nucleus (^{87}Rb) in the extensively studied $RbNO_3$ powder[28,30,38,41,45,51,75,78] was used to illustrate the scaling and labeling of the high-resolution isotropic axis. The acquisition and processing of the data were performed with the hypercomplex or States *et al.* method. We did not synchronize the increment of the experimental evolution period, Δt_1, with the inverse of the rotor spinning rate, ν_{rotor}. If $\Delta t_1=1/\nu_{\text{rotor}}$, then $SW1_{Cz}=\nu_{\text{rotor}}$ for convention Cz and $SW1_{Ck}=\nu_{\text{rotor}}/(1+k)$ for convention Ck. Spinning sidebands along the F_1 dimension, located outside the spectral width SW1, will be folded back onto the centerband, increasing the intensity and improving the line shape of the centerband.[46] However, if ν_{rotor} is not high enough and the spectrum consists of several centerbands, one or several of them can be located outside the spectral width SW1 but still appearing in the spectral width SW1 by folding. As a result, the positions of the center of gravity of these folded centerbands will be erroneous.

Results are presented in Sec. IV. The 2D 3Q-MAS spectrum obtained at 98.2 MHz shows the three peaks of Rb as reported by Massiot *et al.*[41] On the other hand, the spectrum recorded at 163.6 MHz displays only two peaks as reported by Wang *et al.*[38] The true isotropic chemical shifts and the parameters $C_{Q\eta}$ of the three rubidium sites, provided by the two conventions, are in agreement with published data.

II. THEORY

Hamiltonians, carrier frequency, amplitude of rf pulse, and line positions throughout the paper are defined in angular frequency units. Only the offsets are expressed in frequency units. Disregarding relaxation phenomena, the dynamics of a spin I system submitted to a two-pulse sequence [Fig. 1(a)] in NMR experiments is described by the density operator $\rho(t_1,\tau_2,t_3,\tau_4)$ expressed in the rotating frame of ω_0, the latter being a *positive* value. The duration t_1 is that of the first rf pulse, τ_2 is the experimental evolution period, t_3 is the second-pulse duration, and τ_4 is the acquisition period. *In the absence of an rf pulse*, the spin system is submitted to internal interactions H_{int}. As an internal interaction such as the quadrupole interaction[6–14] can be much larger than the coupling of an rf pulse with the spin system, *in the presence of an rf pulse* the spin system is submitted to

$$H=H_{\text{int}}+H_{\text{rf}}, \tag{1}$$

the latter being the Hamiltonian of the rf pulse. As usual, we limit the internal interactions H_{int} to secular Hamiltonians, i.e., those that commute with the Zeeman interaction (the dominant interaction in the NMR spectroscopy), for example, the isotropic chemical shift $H_{\text{CS}}=-\delta_{\text{CS}}^{\text{iso}}\omega_0 I_z$. Since the rf pulse durations are short (some microseconds), the rotor containing the sample appears to be static during the excitation of the spin system by the rf pulses. As a result, the internal interactions remain time independent. Since strong rf pulses are applied, the internal interaction considered during the rf pulses is the first-order quadrupole interaction $H_Q^{(1)\text{static}}$; offset or shift interactions can be neglected.

During the free precession of the spin system, i.e., in the absence of the rf pulses, the chemical shift anisotropy, the first-order quadrupole interaction, as well as $H_{D(IS)}$ are canceled in fast rotating solids at the magic angle, while $H_{D(II)}$ is dramatically reduced. Strictly speaking, the major MAS simplifications occur only for stroscopic observation synchronized with the sample rotation. Furthermore, the MQ-MAS linewidth in the F_1 dimension is largely independent of the magnitude of $H_{D(II)}$.[38] As the main topic of this paper is the MQ-MAS methodology, we consider only the second-order quadrupole interaction for fast rotating solids at the magic angle $H_Q^{(2)\text{fast MAS}}$ and H_{CS} in the remainder of the paper. Therefore,

$$H_{\text{int}}=H_{\text{CS}}+H_Q^{(2)\text{fast MAS}} \tag{2a}$$

during the free precession of the spin system and

$$H=H_Q^{(1)\text{static}}+H_{\text{rf}} \tag{2b}$$

during the rf pulses.

A. Density matrix for an x pulse

We follow the spin dynamics from the thermodynamic equilibrium to the acquisition period using density operators, whose matrix elements, expressed in the eigenstates of I_z, are referred to by two half-integer magnetic numbers r and c for row and column [see Eq. (7)]. The coherence order asso-

ciated with this matrix element is $p=r-c$. By convention, the observable in the acquisition period is the operator $I_+=I_x+iI_y$, which means that the receiver has the coherence order $p=-1$. In the high-temperature approximation, the thermodynamic equilibrium is described by the density operator $\rho(0)=I_z$, whose coherence order is $p=0$. The Hamiltonian of an x pulse is

$$H_{\rm rf}=-\omega_{\rm rf}I_x. \tag{3}$$

At the end of the first rf pulse the density operator is defined by

$$\rho(t_1)=\exp[-i(H_{\rm int}+H_{\rm rf})t_1]\rho(0)\exp[i(H_{\rm int}+H_{\rm rf})t_1]. \tag{4}$$

The matrix form of the interaction H [Eq. (1)] during the x pulse, expressed in the eigenstates of the Zeeman interaction, is not diagonal. The usual procedure is to determine the diagonalized form Ω of H and the transformation operator T related by

$$\Omega=T^{\dagger}HT. \tag{5}$$

Equation (4) is rewritten as

$$\rho(t_1)=T\,\exp(-i\Omega t_1)T^{\dagger}\rho(0)T\,\exp(i\Omega t_1)T^{\dagger}. \tag{6}$$

If Eq. (5) cannot be solved analytically, it can always be solved numerically using standard diagonalization procedure, which is applicable for any half-integer quadrupole spin and whatever the complexity of H [Eq. (1)]. For a spin $I=\frac{3}{2}$ system, the density operator $\rho(t_1)$ has the following general matrix form or density matrix:[12]

$$\rho(t_1)=\begin{array}{c} \\ \langle 3/2| \\ \langle 1/2| \\ \langle -1/2| \\ \langle -3/2| \end{array}\begin{array}{c} \begin{array}{cccc} |3/2\rangle & |1/2\rangle & |-1/2\rangle & |-3/2\rangle \end{array} \\ \begin{bmatrix} \langle I_z^{3/2,-3/2}(t_1)\rangle & \langle I_-^{3/2,1/2}(t_1)\rangle & \langle I_-^{3/2,-1/2}(t_1)\rangle & -i\langle I_y^{3/2,-3/2}(t_1)\rangle \\ \langle I_+^{3/2,1/2}(t_1)\rangle & \langle I_z^{1/2,-1/2}(t_1)\rangle & -i\langle I_y^{1/2,-1/2}(t_1)\rangle & \langle I_-^{1/2,-3/2}(t_1)\rangle \\ \langle I_+^{3/2,-1/2}(t_1)\rangle & i\langle I_y^{1/2,-1/2}(t_1)\rangle & -\langle I_z^{1/2,-1/2}(t_1)\rangle & \langle I_-^{-1/2,-3/2}(t_1)\rangle \\ i\langle I_y^{3/2,-3/2}(t_1)\rangle & \langle I_+^{1/2,-3/2}(t_1)\rangle & \langle I_+^{-1/2,-3/2}(t_1)\rangle & -\langle I_z^{3/2,-3/2}(t_1)\rangle \end{bmatrix} \end{array}, \tag{7}$$

where the matrix element $\langle r|\rho(t_1)|c\rangle$ is the complex (real and imaginary) amplitude of the $(r-c)$-quantum coherence at the end of the rf pulse. For a $p=-1$ quantum coherence, the imaginary part of $\langle r|\rho(t_1)|r+1\rangle$ is proportional to the area of the corresponding absorption line. In the MQ-MAS experiment, rf pulses of various phases are applied. What is the density matrix for an rf pulse of phase φ_1 with respect to an x pulse?

B. Density matrix for an φ_1 pulse

The MQ-MAS methodology cycles the phase of the first rf pulse to selectively detect the desired coherences developed by the first rf pulse in the two-pulse sequence. This section derives the density matrix describing the spin system at the end of the first rf pulse of arbitrary phase. Now the rf magnetic field $\mathbf{B}_1$ is along the x' axis in the rotating frame of ω_0 (Fig. 2). The angle between the x and x' axes is φ_1. The Hamiltonian of an rf pulse of phase φ_1 relative to an x pulse or, in short, a φ_1 pulse is

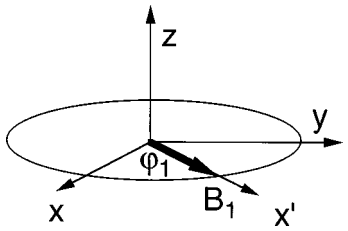

FIG. 2. The angle φ_1 between the x axis and the rf magnetic field $\mathbf{B}_1$ along the x' axis in the rotating frame of the carrier frequency ω_0.

$$H_{\rm rf}^{(\varphi_1)}=-\omega_{\rm rf}I_{x'}, \tag{8}$$

where the operator $I_{x'}$ is the operator I_x expressed along the x' axis. They are related as[3,79,80]

$$I_{x'}=\exp(-i\varphi_1 I_z)I_x\exp(i\varphi_1 I_z) \tag{9}$$

or[81]

$$H_{\rm rf}^{(\varphi_1)}=\exp(-i\varphi_1 I_z)H_{\rm rf}\exp(i\varphi_1 I_z). \tag{10}$$

Since the operators $\exp(-i\varphi_1 I_z)$ and $\exp(i\varphi_1 I_z)$ have no effects on the secular Hamiltonians $H_{\rm int}$, we have

$$H_{\rm int}+H_{\rm rf}^{(\varphi_1)}=\exp(-i\varphi_1 I_z)(H_{\rm int}+H_{\rm rf})\exp(i\varphi_1 I_z). \tag{11}$$

At the end of the φ_1 pulse, the dynamics of the spin system is described by

$$\rho\varphi_1(t_1)=\exp[-i(H_{\rm int}+H_{\rm rf}^{(\varphi_1)})t_1]\rho(0)\times\exp[i(H_{\rm int}+H_{\rm rf}^{(\varphi_1)})t_1]. \tag{12}$$

Because[1,3,4]

$$\exp[-i(H_{\rm int}+H_{\rm rf}^{(\varphi_1)})t_1]=\exp(-i\varphi_1 I_z)\times\exp[-i(H_{\rm int}+H_{\rm rf})t_1]\times\exp(i\varphi_1 I_z), \tag{13}$$

Eq. (12) becomes[81]

$$\begin{aligned}\rho\varphi_1(t_1) &= \exp(-i\varphi_1 I_z)\exp[-i(H_{\rm int}+H_{\rm rf})t_1]\\ &\times\exp(i\varphi_1 I_z)\rho(0)\exp(-i\varphi_1 I_z)\\ &\times\exp[i(H_{\rm int}+H_{\rm rf})t_1]\exp(i\varphi_1 I_z)\\ &= \exp(-i\varphi_1 I_z)\rho(t_1)\exp(i\varphi_1 I_z). \end{aligned} \tag{14}$$

Thus the density operator of a φ_1 pulse is related to that of an x pulse by a simple relation. A matrix element $\langle r|\rho\varphi_1(t_1)|c\rangle$ (written previously as $[\rho\varphi_1(t_1)]_{r,c}$) of $\rho\varphi_1(t_1)$, located at the row and column whose magnetic number is r and c, is related to the same matrix element of $\rho(t_1)$ as

$$\begin{aligned}\langle r|\rho\varphi_1(t_1)|c\rangle &= \langle r|\rho(t_1)|c\rangle\exp[-i(r-c)\varphi_1]\\ &= \langle r|\rho(t_1)|c\rangle\exp(-ip\varphi_1),\end{aligned} \tag{15}$$

or in the matrix form:

$$\rho\varphi_1(t_1) = \begin{array}{c} \\ \langle 3/2| \\ \langle 1/2| \\ \langle -1/2| \\ \langle -3/2| \end{array} \begin{array}{c} \begin{array}{cccc} |3/2\rangle & |1/2\rangle & |-1/2\rangle & |-3/2\rangle \end{array} \\ \begin{bmatrix} \langle I_z^{3/2,-3/2}(t_1)\rangle & \langle I_-^{3/2,1/2}(t_1)\rangle & \langle I_-^{3/2,-1/2}(t_1)\rangle & -i\langle I_y^{3/2,-3/2}(t_1)\rangle \\ & \times e^{-i\varphi_1} & \times e^{-2i\varphi_1} & \times e^{-3i\varphi_1} \\ \langle I_+^{3/2,1/2}(t_1)\rangle & \langle I_z^{1/2,-1/2}(t_1)\rangle & -i\langle I_y^{1/2,-1/2}(t_1)\rangle & \langle I_-^{1/2,-3/2}(t_1)\rangle \\ \times e^{i\varphi_1} & & \times e^{-i\varphi_1} & \times e^{-2i\varphi_1} \\ \langle I_+^{3/2,-1/2}(t_1)\rangle & i\langle I_y^{1/2,-1/2}(t_1)\rangle & -\langle I_z^{1/2,-1/2}(t_1)\rangle & \langle I_-^{-1/2,-3/2}(t_1)\rangle \\ \times e^{2i\varphi_1} & \times e^{i\varphi_1} & & \times e^{-i\varphi_1} \\ i\langle I_y^{3/2,-3/2}(t_1)\rangle & \langle I_+^{1/2,-3/2}(t_1)\rangle & \langle I_+^{-1/2,-3/2}(t_1)\rangle & -\langle I_z^{3/2,-3/2}(t_1)\rangle \\ \times e^{3i\varphi_1} & \times e^{2i\varphi_1} & \times e^{i\varphi_1} & \end{bmatrix} \end{array}. \tag{16}$$

In other words, when an rf pulse is dephased by an angle φ_1, a p-quantum coherence is dephased by $\exp(-ip\varphi_1)$, the spin populations $\langle I_z^{r,-r}(t_1)\rangle$ or zero-quantum coherences are not affected.[1,4] When $\varphi_1=0$, Eq. (16) reduces to Eq. (7). From a practical point of view, it is not necessary to diagonalize the matrix of H for a φ_1 pulse once that of an x pulse is found. Especially for a y pulse, whose matrix contains complex numbers, the numerical diagonalization procedure is more tedious than that of an x pulse, whose matrix contains real numbers only.

After the φ_1 pulse, the spin system is submitted to the internal interactions $H_{\rm int}$. The density operator describing the spin system becomes

$$\rho\varphi_1(t_1,\tau_2) = \exp(-iH_{\rm int}\tau_2)\rho\varphi_1(t_1)\exp(iH_{\rm int}\tau_2). \tag{17}$$

As only secular internal Hamiltonians are considered, the matrix forms of $\exp(-iH_{\rm int}\tau_2)$ and $\exp(iH_{\rm int}\tau_2)$ are diagonal. Using the notation

$$\omega_{r,c} = \langle r|H_{\rm int}|r\rangle - \langle c|H_{\rm int}|c\rangle, \tag{18}$$

the matrix form of $\rho\varphi_1(t_1,\tau_2)$ is

$$\begin{bmatrix} \langle I_z^{3/2,-3/2}(t_1)\rangle & \langle I_-^{3/2,1/2}(t_1)\rangle & \langle I_-^{3/2,-1/2}(t_1)\rangle & -i\langle I_y^{3/2,-3/2}(t_1)\rangle \\ & \times e^{-i\varphi_1} & \times e^{-2i\varphi_1} & \times e^{-3i\varphi_1} \\ & \times e^{-i\tau_2\omega_{3/2,1/2}} & \times e^{-i\tau_2\omega_{3/2,-1/2}} & \times e^{-i\tau_2\omega_{3/2,-3/2}} \\ \langle I_+^{3/2,1/2}(t_1)\rangle & \langle I_z^{1/2,-1/2}(t_1)\rangle & -i\langle I_y^{1/2,-1/2}(t_1)\rangle & \langle I_-^{1/2,-3/2}(t_1)\rangle \\ \times e^{i\varphi_1} & & \times e^{-i\varphi_1} & \times e^{-2i\varphi_1} \\ \times e^{-i\tau_2\omega_{1/2,3/2}} & & \times e^{-i\tau_2\omega_{1/2,-1/2}} & \times e^{-i\tau_2\omega_{1/2,-3/2}} \\ \langle I_+^{3/2,-1/2}(t_1)\rangle & i\langle I_y^{1/2,-1/2}(t_1)\rangle & -\langle I_z^{1/2,-1/2}(t_1)\rangle & \langle I_-^{-1/2,-3/2}(t_1)\rangle \\ \times e^{2i\varphi_1} & \times e^{i\varphi_1} & & \times e^{-i\varphi_1} \\ \times e^{-i\tau_2\omega_{-1/2,3/2}} & \times e^{-i\tau_2\omega_{-1/2,1/2}} & & \times e^{-i\tau_2\omega_{-1/2,-3/2}} \\ i\langle I_y^{3/2,-3/2}(t_1)\rangle & \langle I_+^{1/2,-3/2}(t_1)\rangle & \langle I_+^{-1/2,-3/2}(t_1)\rangle & -\langle I_z^{3/2,-3/2}(t_1)\rangle \\ \times e^{3i\varphi_1} & \times e^{2i\varphi_1} & \times e^{i\varphi_1} & \\ \times e^{-i\tau_2\omega_{-3/2,3/2}} & \times e^{-i\tau_2\omega_{-3/2,1/2}} & \times e^{-i\tau_2\omega_{-3/2,-1/2}} & \end{bmatrix}. \tag{19}$$

TABLE I. All of these parameters depend on the spin I and the coherence order p: $C_0(I,p)$ is defined by Eq. (22b) and $C_2(I,p)$ by Eq. (23b); $\lambda(I,p)=C_0(I,p)/C_0(I,-1)$ is the ratio of the second-order quadrupole shift of the center of gravity of a spectrum generated by a pQ coherence to that of the $-1Q$ coherence [Eq. (25)]; $k(I,p)=-C_2(I,p)/C_2(I,-1)$ defines the echo position; k_{1z} and k_{2z} in Eq. (37) define the observed chemical shift of the center of gravity of the spectrum along the F_1 dimension of a sheared 2D MQ-MAS spectrum labeled using convention Cz [Eq. (69)], k_{1k} and k_{2k} in Eq. (70) are those used with convention Ck; and k_{Gz} and k_{Gk} are defined in Eqs. (72) and (73).

						Convention Cz			Convention Ck		
I	pQ	$C_0(I,p)$	$C_2(I,p)$	$\lambda(I,p)$	$k(I,p)$	k_{1z}	k_{2z}	k_{Gz}	k_{1k}	k_{2k}	k_{Gk}
3/2	$-1Q$	-3	-54								
	$-3Q$	9	42	-3	7/9	34/9	$-20/9$	1/6	17/8	$-5/4$	8/27
5/2	$-1Q$	-8	-144								
	$3Q$	6	228	$-3/4$	19/12	$-17/12$	5/6	$-4/9$	$-17/31$	10/31	$-31/27$
	$-5Q$	50	300	$-25/4$	25/12	85/12	$-25/6$	4/45	85/37	$-50/37$	37/135
7/2	$-1Q$	-15	-270								
	$3Q$	27	606	$-9/5$	101/45	$-34/45$	4/9	$-5/6$	$-17/73$	10/73	$-73/27$
	$5Q$	-15	330	1	11/9	$-34/9$	20/9	$-1/6$	$-17/10$	1	$-10/27$
	$-7Q$	147	966	$-49/5$	161/45	476/45	$-56/9$	5/84	238/103	$-140/103$	103/378
9/2	$-1Q$	-24	-432								
	$3Q$	54	1092	$-9/4$	91/36	$-17/36$	5/18	$-4/3$	$-17/127$	10/127	$-127/27$
	$5Q$	30	1140	$-5/4$	95/36	$-85/36$	25/18	$-4/15$	$-85/131$	50/131	$-131/135$
	$7Q$	-84	168	7/2	7/18	$-119/18$	35/9	$-2/21$	$-119/25$	14/5	$-25/189$
	$-9Q$	324	2232	$-27/2$	31/6	85/6	$-25/3$	2/45	85/37	$-50/37$	37/135

In a single pulse experiment, the $p=-1$ quantum coherences are FID's whose Fourier transformations yield the corresponding absorption lines in the spectrum. The other coherences are not detectable. A second rf pulse is required to convert them to $p=-1$ quantum coherences, as in the MQ-MAS experiment. Equation (19) shows that, except for the zero-quantum coherences, a p-quantum coherence $\langle r|\rho\varphi_1(t_1,\tau_2)|c\rangle$ is characterized by the complex amplitude $\langle r|\rho(t_1)|c\rangle$ and the phase $(p\varphi_1-\tau_2\omega_{r,c})$ of the p-quantum FID following the φ_1 pulse, which are identical to those generated by an x pulse if $\varphi_1=0$. In other words, the Fourier transformation of $\langle r|\rho\varphi_1(t_1,\tau_2)|c\rangle$ with respect to τ_2 yields a p-quantum absorption line, whose area is proportional to the imaginary part of $\langle r|\rho(t_1)|c\rangle$, and whose *position relative to* ω_0 is $\omega_{r,c}$. This absorption line is that generated by an x pulse but modified by the phase φ_1 of the rf pulse. From a theoretical point of view, we can also perform a Fourier transformation of $\langle r|\rho\varphi_1(t_1,\tau_2)|c\rangle$ with respect to φ_1. The ''absorption line'' is located at the position p on the new axis, the coherence order axis; the absorption lines having different p values are split. In short, the double Fourier transformation of $\langle r|\rho\varphi_1(t_1,\tau_2)|c\rangle$ with respect to τ_2 and φ_1 yields a 2D spectrum, whose p-quantum absorption peak is located at $\omega_{r,c}$ along one axis and at p along the other axis.

The contribution of the isotropic chemical shift H_{CS} to the absorption line position with respect to ω_0 is defined by

$$\omega_{r,c}^{(\mathrm{iso})}=\langle r|H_{\mathrm{CS}}|r\rangle-\langle c|H_{\mathrm{CS}}|c\rangle=-(\omega_L-\omega_0)(r-c)=-\delta_{\mathrm{CS}}^{(\mathrm{iso})}\omega_0(r-c), \quad (20a)$$

where $\omega_L=\gamma B_0$ is the Larmor frequency of the nucleus, ω_L being a *positive* number. The analytical expression of $H_Q^{(2)\text{fast MAS}}$ is unknown but is defined by the position of the $(r-c)$-quantum absorption line relative to ω_L or the second-order quadrupole shift $\omega_{r,c}^{(2)\text{fast MAS}}$ of the $(r-c)$-quantum absorption line:

$$\omega_{r,c}^{(2)\text{fast MAS}}=\langle r|H_Q^{(2)\text{fast MAS}}|r\rangle-\langle c|H_Q^{(2)\text{fast MAS}}|c\rangle. \quad (20b)$$

Of course, only $p=-1$-quantum absorption lines are detectable in a single-pulse experiment. Until now, the MQ-MAS methodology has limited the investigation to on-resonance symmetrical coherences, that is, $c=-r$; in this case, $p=2r$ and:[12,82]

$$\omega_{r,-r}^{(2)\text{fast MAS}}=-\frac{\Omega_Q^2}{\omega_0}\left\{\frac{1}{2}C_0B_{0,0}(\eta)+\frac{1}{2}C_2[B_{4,0}(\eta)d_{0,0}^{(4)}(\beta_1)+2B_{4,2}(\eta)d_{2,0}^{(4)}(\beta_1)\cos 2\alpha_1+2B_{4,4}(\eta)d_{4,0}^{(4)}\times(\beta_1)\cos 4\alpha_1]P_4(\cos\theta_m)\right\}, \quad (21a)$$

with

$$\Omega_Q=\frac{e^2qQ}{2I(2I-1)\hbar}. \quad (21b)$$

The two parameters C_0 and C_2, given in Table I, can be expressed as functions of either I and r or I and p:[12,32]

$$C_0(I,r)=-C_0(I,-r)=2r[I(I+1)-3r^2], \quad (22a)$$

$$C_0(I,p)=-C_0(I,-p)=p[I(I+1)-\tfrac{3}{4}p^2], \quad (22b)$$

$$C_2(I,r)=-C_2(I,-r)=2r[18I(I+1)-34r^2-5], \quad (23a)$$

$$C_2(I,p)=-C_2(I,-p)=p[18I(I+1)-\tfrac{17}{2}p^2-5]. \quad (23b)$$

The other parameters in Eq. (21a) were defined previously.[12] In particular, the second-order quadrupole shift of the center of gravity of the central line ($r=-\frac{1}{2}$) is

$$\omega_{-1/2,1/2}^{(2)\mathrm{iso}}=-\frac{3\Omega_Q^2}{10\omega_0}\left[I(I+1)-\frac{3}{4}\right]\left(1+\frac{1}{3}\,\eta^2\right); \quad (24)$$

that of an on-resonance symmetrical coherence is

$$\omega_{r,-r}^{(2)\mathrm{iso}}=\lambda\,\omega_{-1/2,1/2}^{(2)\mathrm{iso}}. \quad (25)$$

The parameter λ, given in Table I, can also be expressed in two ways:

$$\lambda(I,r)=-\lambda(I,-r)=\frac{C_0(I,r)}{C_0(I,-1/2)}, \quad (26a)$$

$$\lambda(I,p)=-\lambda(I,-p)=\frac{C_0(I,p)}{C_0(I,-1)}. \quad (26b)$$

The parameters $C_0(I,p)$, $C_2(I,p)$, and $\lambda(I,p)$ are odd functions of the coherence order p. If η cannot be determined by line-shape analysis, the parameter $C_{Q\eta}$ relating e^2qQ/h and η, derived from Eqs. (21b) and (24), is used for characterizing a material:

$$C_{Q\eta}=\frac{e^2qQ}{h}\sqrt{\eta^2/3+1}$$

$$=I(2I-1)\,\frac{\omega_0}{2\pi}\sqrt{\frac{40}{3[I(I+1)-3/4]}\left[-\frac{\omega_{-1/2,1/2}^{(2)\mathrm{iso}}}{\omega_0}\right]}. \quad (26c)$$

C. Selective detection of the ±3-quantum coherences generated by the first rf pulse

As only $p=-1$ quantum coherences are detected, a second rf pulse is required to convert the MQ coherences developed by the first rf pulse to $p=-1$ quantum coherences. This conversion is described by

$$\rho\varphi_1(t_1,\tau_2,t_3)=T\,\exp(-i\Omega t_3)T^{\dagger}\rho\varphi_1(t_1,\tau_2)T \times\exp(i\Omega t_3)T^{\dagger}. \quad (27)$$

To detect the ±3-quantum coherences selectively, we have to phase cycle the first rf pulse. According to Eq. (15), the $p=\pm3$ quantum coherences remain unchanged if $\varphi_1=0$, $2\pi/3$, or $4\pi/3$. On the other hand, the $p=\pm2$ and ±1 quantum coherences are affected by these three phases. For each of these four coherences, the phase function $\exp(-ip\varphi_1)$ takes three values: 1, $\exp(i2\pi/3)$, and $\exp(i4\pi/3)$. These three complex numbers may be thought of as three vectors in the complex plane which, when adding the tail of one to the head of the previous one, form the sides of a triangle, giving a zero result,[79] i.e., $1+\exp(i2\pi/3)+\exp(i4\pi/3)=0$. Phase cycling the first rf pulse by the angles $\varphi_1=0°$, 120°, and 240° and coadding the three contributions is equivalent to starting with the following matrix form of $\rho\varphi_1(t_1,\tau_2)$:

$$\begin{bmatrix} \langle I_z^{3/2,-3/2}(t_1)\rangle & 0 & 0 & -i\langle I_y^{3/2,-3/2}(t_1)\rangle e^{-i\tau_2\omega_{3/2,-3/2}} \\ 0 & \langle I_z^{1/2,-1/2}(t_1)\rangle & 0 & 0 \\ 0 & 0 & -\langle I_z^{1/2,-1/2}(t_1)\rangle & 0 \\ i\langle I_y^{3/2,-3/2}(t_1)\rangle e^{-i\tau_2\omega_{-3/2,3/2}} & 0 & 0 & -\langle I_z^{3/2,-3/2}(t_1)\rangle \end{bmatrix}. \quad (28a)$$

The $p=\pm1$ and ±2 quantum coherences are canceled by the three phase cyclings of the first rf pulse. Unfortunately, the zero-quantum coherences are preserved. As $\exp(i\pi/6)+\exp(i\pi/2)+\exp(i5\pi/6)=0$, a new three-phase cycling, consisting of the angles $\varphi_1=30°$, 90°, and 150°, generates the following matrix form of $\rho\varphi_1(t_1,\tau_2)$:

$$\begin{bmatrix} \langle I_z^{3/2,-3/2}(t_1)\rangle & 0 & 0 & i\langle I_y^{3/2,-3/2}(t_1)\rangle e^{-i\tau_2\omega_{3/2,-3/2}} \\ 0 & \langle I_z^{1/2,-1/2}(t_1)\rangle & 0 & 0 \\ 0 & 0 & -\langle I_z^{1/2,-1/2}(t_1)\rangle & 0 \\ -i\langle I_y^{3/2,-3/2}(t_1)\rangle e^{-i\tau_2\omega_{-3/2,3/2}} & 0 & 0 & -\langle I_z^{3/2,-3/2}(t_1)\rangle \end{bmatrix}. \quad (28b)$$

The second three-phase cycling keeps the ±3- and zero-quantum coherences and cancels ±1- and ±2-quantum coherences as in the previous case, but the signs of the ±3-quantum coherences are reversed. Those of the zero-quantum coherences are unchanged. To cancel these unwanted contributions of the zero-quantum coherences, the receiver phase associated with the second sequence must be reversed before coadding the two results [Fig. 1(e)]. This sequence consists of six phase cyclings.[32,34,41] In this case only the ±3-quantum coherences are preserved. We need to consider the following density matrix $\rho(t_1,\tau_2)$:

$$\begin{bmatrix} 0 & 0 & 0 & i\langle I_y^{3/2,-3/2}(t_1)\rangle e^{-i\tau_2\omega_{3/2,-3/2}} \\ 0 & 0 & 0 & 0 \\ 0 & 0 & 0 & 0 \\ -i\langle I_y^{3/2,-3/2}(t_1)\rangle e^{-i\tau_2\omega_{-3/2,3/2}} & 0 & 0 & 0 \end{bmatrix}, \tag{28c}$$

for $\rho\varphi_1(t_1,\tau_2)$ in Eq. (27). The latter becomes independent of φ_1 and can be written as

$$\rho(t_1,\tau_2,t_3)=T\ \exp(-i\Omega t_3)T^{\dagger}\rho(t_1,\tau_2)T\ \exp(i\Omega t_3)T^{\dagger}. \tag{29}$$

The two matrix elements in Eq. (28c) contribute to the complex amplitude of the FID following the second rf pulse and to that of the echo. For a spin $I=\frac{3}{2}$, both ± 3-quantum coherences are represented by a single matrix element. For the other half-integer quadrupole spins, it is not the case. This is why only on-resonance symmetrical coherences are studied, considering only a single matrix element for a given MQ coherence order.

D. Echo and antiecho pathways for a spin $I=\frac{3}{2}$ system

As the present paper deals with the MQ-MAS technique applied to a spin $I=\frac{3}{2}$ system using the two-pulse sequence, the first rf pulse is of phase φ_1; that of the second is an x pulse or $\varphi_2=0$. We consider only the matrix elements associated with the $p=\pm 3$ quantum coherences developed at the end of the first rf pulse [Fig. 3(a)] or Eq. (28c) with $\tau_2=0$. The time-domain signal $\langle -\frac{1}{2}|\rho^S(t_1,\tau_2,t_3,\tau_4)|\frac{1}{2}\rangle$ during the acquisition period τ_4, described by the simplified density operator $\rho^S(t_1,\tau_2,t_3,\tau_4)$, was obtained previously from a detailed development,[12]

$$\langle -\tfrac{1}{2}|\rho^S(t_1,\tau_2,t_3,\tau_4)|\tfrac{1}{2}\rangle = \exp(-i\tau_4\omega^{\text{fast MAS}}_{-1/2,1/2})\sum_{p=-3,3}\langle -\tfrac{1}{2}|\rho_p^S(t_1,t_3)|\tfrac{1}{2}\rangle \times \exp(-i\tau_2\omega^{\text{fast MAS}}_{p/2,-p/2}). \tag{30}$$

The superscript S means ''simplified'' and

$$\rho_p^S(t_1,t_3)=T\ \exp(-i\Omega t_3)T^{\dagger}\rho_p^S(t_1)T\ \exp(i\Omega t_3)T^{\dagger}, \tag{31}$$

$$\omega^{\text{fast MAS}}_{p/2,-p/2}=\lambda(I,p)\omega^{(2)\text{iso}}_{-1/2,1/2}-k(I,p)\xi_{-1/2,1/2}-p\,\delta^{(\text{iso})}_{\text{CS}}\omega_0, \tag{32}$$

$$k(I,p)=-k(I,-p)=-\frac{C_2(I,p)}{C_2(I,-1)}. \tag{33}$$

The parameter $\xi_{-1/2,1/2}$ is related to the width of the central line of a powder sample.[12] The other two parameters, $\lambda(I,p)$ and $k(I,p)$, were previously defined for the four half-integer quandrupole spins.[12] Those related to MQ-MAS methodology are reported in Table I. For the $p=-1$ quantum coherences, which are detected during the acquisition period, Eq. (32) becomes

$$\omega^{\text{fast MAS}}_{-1/2,1/2}=\omega^{(2)\text{iso}}_{-1/2,1/2}+\xi_{-1/2,1/2}+\delta^{(\text{iso})}_{\text{CS}}\omega_0. \tag{34}$$

For $I=\frac{3}{2}$ and $p=-3$, we have $\lambda=-3$ and $k=\frac{7}{9}$. Equation (30) is rewritten as

$$\langle -\tfrac{1}{2}|\rho^S(t_1,\tau_2,t_3,\tau_4)|\tfrac{1}{2}\rangle=\sum_{p=-3,3}\langle -\tfrac{1}{2}|\rho_p^S(t_1,t_3)|\tfrac{1}{2}\rangle\exp\{-i\omega^{(2)\text{iso}}_{-1/2,1/2}[\tau_4+\lambda(I,p)\tau_2]\} \times\exp\{-i\xi_{-1/2,1/2}[\tau_4-k(I,p)\tau_2]\}\exp[-i\delta^{(\text{iso})}_{\text{CS}}\omega_0(\tau_4-p\tau_2)]. \tag{35}$$

The MQ-MAS methodology is concerned with the condition $\tau_4=k(I,p)\tau_2$; in this case the effects of $\xi_{-1/2,1/2}$ are canceled,

$$\langle -\tfrac{1}{2}|\rho^S(t_1,\tau_2,t_3,\tau_4=k(I,p)\tau_2)|\tfrac{1}{2}\rangle = \sum_{p=-3,3}\langle -\tfrac{1}{2}|\rho_p^S(t_1,t_3)|\tfrac{1}{2}\rangle\exp[-i\tau_2\omega_{F_1}(I,p)], \tag{36}$$

with

$$\omega_{F_1}(I,p)=\omega^{(2)\text{iso}}_{-1/2,1/2}[k(I,p)+\lambda(I,p)]+\delta^{(\text{iso})}_{\text{CS}}\omega_0[k(I,p)-p] =k_{1z}\delta^{(\text{iso})}_{\text{CS}}\omega_0+k_{2z}\omega^{(2)\text{iso}}_{-1/2,1/2}. \tag{37}$$

The two parameters k_{1z} and k_{2z} are reported in Table I for the four half-integer quadrupole spins. Equation (36) consists of two terms. Their expressions are similar to a matrix element of $\rho\varphi_1(t_1,\tau_2)$ in Eq. (19) with $\varphi_1=0$. In other words,

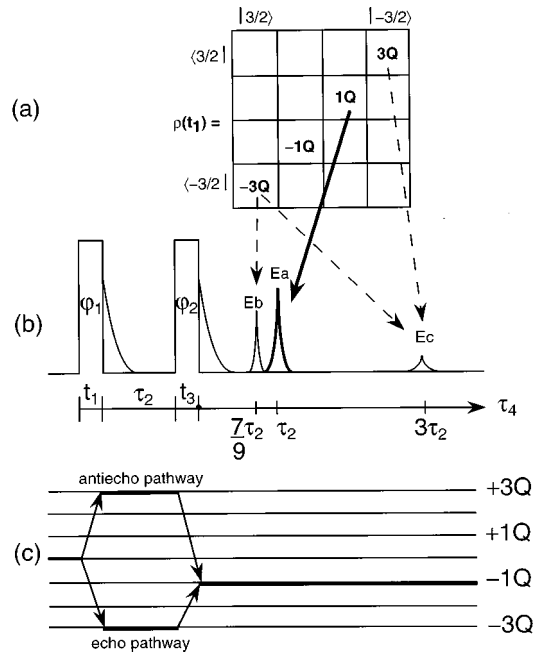

FIG. 3. (a) The elements of the density matrix at the end of the first rf pulse that contribute to the echoes and antiechoes for a spin $I=\frac{3}{2}$ system. (b) Three echoes (Ref. 12) are predicted for a spin $I=\frac{3}{2}$ system, submitted to the isotropic chemical shift and the second-order quadrupole interaction, in a fast rotating sample at the magic angle: Ea is the usual Hahn echo, Eb the echo involved in the 3Q-MAS methodology, and Ec a predicted echo not yet observed experimentally. (c) The echo and antiecho pathways associated with the 3Q-MAS experiment of a spin $I=\frac{3}{2}$ system.

$\langle -\frac{1}{2}|\rho_p^S(t_1,t_3)|\frac{1}{2}\rangle$, which depends on the two rf pulse durations, and $\tau_2\omega_{F_1}(I,p)$ are the complex amplitude and the phase of the signal at $\tau_4=k(I,p)\tau_2$, respectively. The Fourier transformation of Eq. (36) with respect to the experimental evolution period τ_2 yields *two absorption lines located at the positions* $\omega_{F_1}(I,p)$ *relative to* ω_0. *In fact,* $\omega_{F_1}(I,p)$ *represents the position of the center of gravity of an MQ-filtered central-transition peak relative to* ω_0 *in the* F_1 *dimension of a 2D MQ-MAS spectrum* (see Sec. II F). The line position $\omega_{F_1}(I,p)$ depends only on two isotropic values, $\omega^{(2)\text{iso}}_{-1/2,1/2}$ and $\delta^{(\text{iso})}_{\text{CS}}$; therefore, Eq. (37) is valid for a single crystal as well as a powder sample. The acquisition of the time-domain signals is supposed to start at the echo position $\tau_4=k(I,p)\tau_2$ or the top of the echo. In the MQ-MAS experiment, this is not the case since the acquisition period starts at the end of the second rf pulse. As a result, the 2D spectrum is tilted (see Sec. II E).

Our approach to determining the position of the center of gravity $\omega_{F_1}(I,p)$ of an MQ-filtered central-transition peak differs with those of Nagayama *et al.*,[83] Grandinetti *et al.*,[84] Hanaya and Harris,[45] Medek *et al.*,[32] and Massiot *et al.*[41] As $k(I,p)$ and $\lambda(I,p)$ are odd functions of p [see Eqs. (26b) and (36)], they have opposite signs for the ± 3-quantum coherences. For the coherence transfer pathway $0\rightarrow(p=-3)\rightarrow-1$, an echo located at $\tau_4=\frac{7}{9}\tau_2$ is observed in the acquisition period [Fig. 3(b)], and the pathway is called the echo pathway [Fig. 3(c)]. Equation (36) becomes

$$\langle -\tfrac{1}{2}|\rho^{\text{Echo}}\left(t_1,\tau_2,t_3,\tau_4=\tfrac{7}{9}\tau_2\right)|\tfrac{1}{2}\rangle = \langle -\tfrac{1}{2}|\rho^S_{-3}(t_1,t_3)|\tfrac{1}{2}\rangle \exp[-i\tau_2\omega_{F_1}(I,p)]. \quad (38)$$

For the coherence transfer pathway $0\rightarrow(p=+3)\rightarrow-1$, Eq. (36) becomes

$$\langle -\tfrac{1}{2}|\rho^{\text{Antiecho}}(t_1,\tau_2,t_3,\tau_4=-\tfrac{7}{9}\tau_2)|\tfrac{1}{2}\rangle = \langle -\tfrac{1}{2}|\rho^S_3(t_1,t_3)|\tfrac{1}{2}\rangle \exp[i\tau_2\omega_{F_1}(I,p)]; \quad (39)$$

an antiecho in the evolution period, located at $\tau_4=-\frac{7}{9}\tau_2$, is predicted and the pathway is called the antiecho pathway [Fig. 3(c)]. Unfortunately, these definitions for the echo and antiecho pathways are not universally accepted.[45] Equations (38) and (39) show that the complex amplitudes of the echo and antiecho are *phase modulated* by $\exp[-i\tau_2\omega_{F_1}(I,p)]$ and $\exp[i\tau_2\omega_{F_1}(I,p)]$, respectively. Since $\rho^S_p(t_1)=-\rho^S_{-p}(t_1)$, the imaginary parts of $\langle -\frac{1}{2}|\rho^S_3(t_1,t_3)|\frac{1}{2}\rangle$ and $\langle -\frac{1}{2}|\rho^S_{-3}(t_1,t_3)|\frac{1}{2}\rangle$ have opposite amplitudes of different magnitudes, because the difference between the initial and final coherence orders is 4 and -2 for 3-quantum and -3-quantum coherences, respectively. Thus the echo and the antiecho have opposite amplitudes of different magnitudes. If they have the same magnitude, their sum is *amplitude modulated* by the sine function, whereas their difference is *amplitude modulated* by the cosine function.

For the four half-integer quadrupole spins, the coherence transfer pathway $0\rightarrow(p=-2I)\rightarrow-1$ is the echo pathway and $0\rightarrow(p=2I)\rightarrow-1$ the antiecho pathway. For the other coherences $(p\neq\pm 2I)$, in contrast, the coherence transfer pathway $0\rightarrow(p<0)\rightarrow-1$ is the antiecho pathway and $0\rightarrow(p>0)\rightarrow-1$ the echo pathway. This is due to the fact that the coherence following the echo pathway precesses with angular frequencies of opposite signs in the experimental evolution and acquisition periods. On the other hand, the coherence following the antiecho pathway precesses with angular frequencies of the same sign in both periods.

Table II presents the phases of the two rf pulses and those of the receiver that generate the quadrature detection for the F_1 dimension. The procedure used is the hypercomplex or States *et al.* method.[41,77] This method generates two series of files called the cosine part $S^{(\cos)}(\tau_2,\tau_4)$ and sine part $S^{(\sin)}(\tau_2,\tau_4)$. These two files are, as mentioned above, a combination of the echo and antiecho signals:

$$S^{(\cos)}(\tau_2,\tau_4)=\frac{1}{2}\left[f^{(\text{Echo})}(\tau_2,\tau_4)-f^{(\text{Antiecho})}(\tau_2,\tau_4)\right], \quad (40)$$

$$iS^{(\sin)}(\tau_2,\tau_4)=\frac{1}{2}\left[f^{(\text{Echo})}(\tau_2,\tau_4)+f^{(\text{Antiecho})}(\tau_2,\tau_4)\right]. \quad (41)$$

The factors 1/2 are included for convenience, so that inversely

$$f^{(\text{Echo})}(\tau_2,\tau_4)=S^{(\cos)}(\tau_2,\tau_4)+iS^{(\sin)}(\tau_2,\tau_4), \quad (42)$$

$$f^{(\text{Antiecho})}(\tau_2,\tau_4)=-S^{(\cos)}(\tau_2,\tau_4)+iS^{(\sin)}(\tau_2,\tau_4). \quad (43)$$

TABLE II. The phase of the first rf pulse φ_1 and the receiver phase φ_r involved in the two-pulse 3Q-MAS sequence applied to a spin $I=\frac{3}{2}$ system, using the hypercomplex (Ref. 41) or States *et al.* method for generating quadrature detection in the t_1 domain that consists of two parts: the cosine part and the sine part. The phases are expressed in degrees (0 means $+x$ pulse or receiver in $+x$ direction). The phase of the second rf pulse φ_2 remains equal to 0. The echo pathway is that of the $-3Q$ coherence whereas the antiecho pathway is that of the $3Q$ coherence (see Fig. 3). The receiver phase is given by $\varphi_r=\Sigma_{i=1}^{2}(p_{i-}-p_{i+})\varphi_i$, where p_{i-} and p_{i+} are the coherence orders before and after the ith rf pulse (Ref. 1). For the cosine part of the quadrature detection along the F_1 dimension, the receiver phase of the echo pathway is $\varphi_r=3\varphi_1-2\varphi_2$ whereas the receiver phase of the antiecho pathway is $\varphi_r=-3\varphi_1+4\varphi_2$. For the sine part of the quadrature detection along the F_1 dimension, the phase of the first rf pulse is delayed of 30° relative to that of the cosine part according to the rule $\pi/(2p)$ or $90°/p$, in the present case $p=-3$. The four receiver lists φ_r show that the signal associated with the cosine part of the quadrature detection is equal to the echo signal *minus* (opposite receiver phase lists) the antiecho signal; the signal associated with the sine part of the quadrature detection is equal to the echo signal *plus* (same receiver phase list) the antiecho signal. The experimental receiver-phase lists for the cosine part and the sine part of the quadrature detection are that of the cosine part of the echo: {90, 270, 90, 270, 90, 270}. It is understood that the signals associated with the cosine part and the sine part of the quadrature detection are acquired in simultaneous mode.

Quadrature detection along the F_1 dimension	Pathway	φ_1						φ_2	φ_r					
Cosine part	Echo	30	90	150	210	270	330	0	90	270	90	270	90	270
	Antiecho	30	90	150	210	270	330	0	−90	−270	−90	−270	−90	−270
Sine part	Echo	0	60	120	180	240	300	0	0	180	0	180	0	180
	Antiecho	0	60	120	180	240	300	0	0	180	0	180	0	180

In practice, the cosine and sine parts are acquired consecutively for the same experimental evolution period, i.e., the acquisition for the F_1 dimension is in the simultaneous mode. Once the experiment is finished, the first data processing is to separate the series of data into two independent files called $S^{(\cos)}(\tau_2,\tau_4)$ and $S^{(\sin)}(\tau_2,\tau_4)$. As the complex number i in Eq. (41) is not generated during the experiment, because the experimental receiver phase was that of the cosine part of the echo (see Table II) and was used for both the cosine and sine parts of the echo, the complex number i is introduced afterwards. Multiplying $S^{(\sin)}(\tau_2,\tau_4)$ by $\exp(i\pi/2)$ to generate the complex number i and adding it to $S^{(\cos)}(\tau_2,\tau_4)$ yield a new file called $f^{(\mathrm{Echo})}(\tau_2,\tau_4)$ or Eq. (42). Similarly, multiplying $S^{(\cos)}(\tau_2,\tau_4)$ by $\exp(i\pi)$ to generate the minus sign in Eq. (43) and adding it to the previously transformed file $iS^{(\sin)}(\tau_2,\tau_4)$ yields a new file called $f^{(\mathrm{Antiecho})}(\tau_2,\tau_4)$ or Eq. (43). The complex number i can be generated during the experiment if the experimental receiver phase for the sine part, i.e., {0,180,0,180,0,180}, is included in the pulse program and used to detect the sine part.

In fact Eq. (37) is valid for the usual Hahn echo located at $\tau_4=\tau_2$ [Fig. 3(b)].[12] As mentioned above, the echo pathway is $0\rightarrow 1\rightarrow -1$, whereas the antiecho pathway is $0\rightarrow -1\rightarrow -1$. In this case $p=k=1$ and $\lambda=-1$ for the four half-integer quadrupole spins.[12] As a result, $\omega_{F_1}(I,\ p=1)=0$. The MQ-MAS methodology applied to the $\tau_4=\tau_2$ Hahn echoes will not resolve peaks along the F_1 dimension. At this point in data processing, we have two time-domain files $f^{(\mathrm{Echo})}(\tau_2,\tau_4)$ and $f^{(\mathrm{Antiecho})}(\tau_2,\tau_4)$.

E. Shearing transformation

This section shows why a 2D MQ-MAS spectrum is normaly tilted and presents the shearing transformation which yields a high-resolution spectrum along the F_1 dimension. In the remainder of the paper, we adopt the notations commonly used in the literature. Figure 1 lists the different notations. From now on, the time-domain parameter t_1 is not the first-pulse duration any more but describes the experimental or MQ coherence evolution period. The acquisition period is represented by t_2, which starts at the end of the second rf pulse. These two experimental parameters (t_1,t_2) are indeed used for the setup of the data acquisition [Fig. 1(b)].

For simplicity, we model the echo signal $f^{(\mathrm{Echo})}(t_1,t_2)$ by the amplitude $A^{(\mathrm{Echo})}(t_2-kt_1)$ of the echo located at $t_2=kt_1$ and the phase $a(t_1)$ of this echo amplitude, and the antiecho signal $f^{(\mathrm{Antiecho})}(t_1,t_2)$ by the amplitude $A^{(\mathrm{Antiecho})}(t_2+kt_1)$ of the antiecho located at $t_2=-kt_1$ and the phase $a(-t_1)$ of this antiecho amplitude. The phase function is of the form $a(t_1)=\exp[-it_1\omega_{F_1}(I,p)]$ as in Eqs. (36) and (38). The echo and antiecho amplitude functions could be modeled by the classical functions $A^{(\mathrm{Echo})}(t_2-kt_1)=\exp(-|t_2-kt_1|/T_{2p})$ and $A^{(\mathrm{Antiecho})}(t_2+kt_1)=\exp(-|t_2+kt_1|/T_{2p})$, where T_{2p} is the spin-spin relaxation time of the coherence with order p. In fact this is not necessary. We need to consider the general properties of the echo and antiecho amplitudes. The echo amplitude $A^{(\mathrm{Echo})}(t_2-kt_1)$ is an extremum at the echo position $t_2=kt_1$. Furthermore, we assume that they are far from the second rf pulse and that $A^{(\mathrm{Echo})}(t_2-kt_1)$ and $A^{(\mathrm{Antiecho})}(t_2+kt_1)$ are symmetrical functions of time as shown in Fig. 1(a) for the echo. Of course, the echo and antiecho amplitudes also depend on the two rf pulse durations [see Eqs. (38) and (39)]. As the latter are constant throughout the experiment, they are not taken into account explicitly thereafter. Hence the echo sig-

nal $f^{(\mathrm{Echo})}(t_1,t_2)$ and the antiecho signal $f^{(\mathrm{Antiecho})}(t_1,t_2)$ are approximated as products of two functions:

$$f^{(\mathrm{Echo})}(t_1,t_2)=A^{(\mathrm{Echo})}(t_2-kt_1)a(t_1), \tag{44}$$

$$f^{(\mathrm{Antiecho})}(t_1,t_2)=A^{(\mathrm{Antiecho})}(t_2+kt_1)a(-t_1). \tag{45}$$

The echo and antiecho signals are functions of two time-domain parameters t_1 and t_2, which are not independent but are related in so far as they are the variables of the amplitude functions. In a 2D representation where the y axis is t_1 and the x axis is t_2, $1/k$ is the slope of the echo position in $f^{(\mathrm{Echo})}(t_1,t_2)$ and $-1/k$ is the slope of the antiecho position in $f^{(\mathrm{Antiecho})}(t_1,t_2)$.[11,31,32,51,76]

1. Unsheared spectra

The Fourier transformation of $f^{(\mathrm{Echo})}(t_1,t_2)$ and $f^{(\mathrm{Antiecho})}(t_1,t_2)$ with respect to the acquisition period t_2 generates two new functions $f^{(\mathrm{Echo})}(t_1,\omega_2)$ and $f^{(\mathrm{Antiecho})}(t_1,\omega_2)$ of time- and frequency-domain parameters t_1 and ω_2, respectively:

$$f^{(\mathrm{Echo})}(t_1,\omega_2)=a(t_1)\int_0^{+\infty}A^{(\mathrm{Echo})}(t_2-kt_1)\exp(-i\omega_2t_2)dt_2, \tag{46}$$

$$f^{(\mathrm{Antiecho})}(t_1,\omega_2)=a(-t_1)\int_0^{+\infty}A^{(\mathrm{Antiecho})}(t_2+kt_1)\times\exp(-i\omega_2t_2)dt_2. \tag{47}$$

Consider Eq. (46): as we assume the echo is far from the second rf pulse so that the full echo is observed, the lower bound of the integral can be extended from zero to minus infinity. Then we make the variable change $t_2'=t_2-kt_1$. Finally we divide the time domain into two parts:

$$f^{(\mathrm{Echo})}(t_1,\omega_2)=a(t_1)\exp(-i\omega_2kt_1)\left(\int_{-\infty}^{0}A^{(\mathrm{Echo})}(t_2')\exp(-i\omega_2t_2')dt_2'+\int_0^{+\infty}A^{(\mathrm{Echo})}(t_2')\exp(-i\omega_2t_2')dt_2'\right). \tag{48}$$

We change the sign of t_2' in the first integral of Eq. (48), i.e., t_2' becomes $-t_2'$. Taking into account that $A^{(\mathrm{Echo})}(-t_2')=A^{(\mathrm{Echo})}(t_2')$, Eq. (48) becomes

$$\begin{aligned}f^{(\mathrm{Echo})}(t_1,\omega_2)&=a(t_1)\exp(-i\omega_2kt_1)\left(\int_0^{+\infty}A^{(\mathrm{Echo})}(t_2')\exp(i\omega_2t_2')dt_2'+\int_0^{+\infty}A^{(\mathrm{Echo})}(t_2')\exp(-i\omega_2t_2')dt_2'\right)\\&=a(t_1)\exp(-i\omega_2kt_1)[A_2^{(\mathrm{Echo})}(-\omega_2)+iD_2^{(\mathrm{Echo})}(-\omega_2)+A_2^{(\mathrm{Echo})}(\omega_2)+iD_2^{(\mathrm{Echo})}(\omega_2)].\end{aligned} \tag{49}$$

The absorption $A_2^{(\mathrm{Echo})}(\omega_2)$ and dispersion $D_2^{(\mathrm{Echo})}(\omega_2)$ spectra are even and odd functions of ω_2, respectively. They result from the Fourier transformation of $A^{(\mathrm{Echo})}(t_2')$ where the time-domain variable is t_2' instead of t_2 as in Eq. (46). That is, *the Fourier transform of the echo signal starts at the top of the echo*. Thus

$$f^{(\mathrm{Echo})}(t_1,\omega_2)=2a(t_1)\exp(-i\omega_2kt_1)A_2^{(\mathrm{Echo})}(\omega_2). \tag{50}$$

Similarly for the antiecho signal [Eq. (47)] we have

$$f^{(\mathrm{Antiecho})}(t_1,\omega_2)=2a(-t_1)\exp(i\omega_2kt_1)A_2^{(\mathrm{Antiecho})}(\omega_2). \tag{51}$$

Equations (50) and (51) show that the absorption spectra of $f^{(\mathrm{Echo})}(t_1,\omega_2)$ and $f^{(\mathrm{Antiecho})}(t_1,\omega_2)$ in the F_2 dimension, which is described by ω_2, will be $A_2^{(\mathrm{Echo})}(\omega_2)$ and $A_2^{(\mathrm{Antiecho})}(\omega_2)$ if the latter are not modified by $\exp(-i\omega_2kt_1)$ for the echo signal and by $\exp(i\omega_2kt_1)$ for the antiecho signal. This occurs if the acquisition period starts at the top of the echo. In the 1D experiment, taking the magnitude representation of the echo signal $f^{(\mathrm{Echo})}(t_1,\omega_2)$ generates a pure absorption spectrum, canceling the effect of $\exp(-i\omega_2kt_1)a(t_1)$.[43,51,85] However, a factor such as minus one or $a(t_1)$, if present, is lost by this processing. Of course the expression of the echo signal differs with Eq. (50) when the full echo signal is not detected. This occurs when the experimental evolution period is shorter than the FID duration. In a 2D representation of the absorption spectra of $f^{(\mathrm{Echo})}(t_1,\omega_2)$ and $f^{(\mathrm{Antiecho})}(t_1,\omega_2)$ for increasing values of t_1, the effects of the functions $\exp(-i\omega_2kt_1)$ and $\exp(i\omega_2kt_1)$ are negligible when the experimental evolution period t_1 is short but become significant for longer durations of t_1.[11,32,76]

If we proceed further in applying the Fourier transformation to $f^{(\mathrm{Echo})}(t_1,\omega_2)$ and $f^{(\mathrm{Antiecho})}(t_1,\omega_2)$ with respect to the experimental evolution period t_1, two new functions $f^{(\mathrm{Echo})}(\omega_1,\omega_2)$ and $f^{(\mathrm{Antiecho})}(\omega_1,\omega_2)$ of two frequency-domain parameters ω_1 and ω_2 or two 2D spectra are generated:

$$f^{(\mathrm{Echo})}(\omega_1,\omega_2)=2A_2^{(\mathrm{Echo})}(\omega_2)S_1^{(\mathrm{Echo})}(\omega_1+k\omega_2), \tag{52}$$

$$f^{(\mathrm{Antiecho})}(\omega_1,\omega_2)=2A_2^{(\mathrm{Antiecho})}(\omega_2)S_1^{(\mathrm{Antiecho})}(\omega_1-k\omega_2), \tag{53}$$

with

$$S_1^{(\mathrm{Echo})}(\omega_1+k\omega_2)=\int_0^{+\infty}a(t_1)\exp[-i(\omega_1+k\omega_2)t_1]dt_1, \tag{54}$$

$$S_1^{(\text{Antiecho})}(\omega_1-k\omega_2)=\int_0^{+\infty}a(-t_1)\times\exp[-i(\omega_1-k\omega_2)t_1]dt_1. \tag{55}$$

Equations (52) and (53) show that the 2D spectra are products of two functions like Eqs. (44) and (45). The spectra along the F_2 dimension depend only on ω_2. The spectra along the F_1 dimension [Eqs. (54) and (55)], described by ω_1, depend also on the frequency ω_2 of the F_2 dimension, *which makes the 2D spectra tilted*. The spectra show a correlation of MQ coherences in the F_1 dimension with SQ coherences in the F_2 dimension. In other words, the frequencies ω_1 and ω_2 are also not independent. *The tilting of spectra is due to the experimental data acquisition, which starts at the end of the second rf pulse*. Fernandez *et al.*[65–67] present a detailed analysis of this kind of 2D spectrum to extract the quadrupole parameters.

2. Sheared spectra

To make the F_1 dimension a high-resolution isotropic dimension, *before the Fourier transformation with respect to* t_1, the function $f^{(\text{Echo})}(t_1,\omega_2)$ is multiplied by $\exp(i\omega_2 k t_1)$ to cancel $\exp(-i\omega_2 k t_1)$ and $f^{(\text{Antiecho})}(t_1,\omega_2)$ is multiplied by $\exp(-i\omega_2 k t_1)$ to cancel $\exp(i\omega_2 k t_1)$, which corresponds to a first-order phase correction.[75] *This transformation is called shearing*. The functions $f^{(\text{Echo})}(t_1,\omega_2)$ and $f^{(\text{Antiecho})}(t_1,\omega_2)$ become two new functions $f_s^{(\text{Echo})}(t_1,\omega_2)$ and $f_s^{(\text{Antiecho})}(t_1,\omega_2)$ where the subscript s means sheared:

$$f_s^{(\text{Echo})}(t_1,\omega_2)=2a(t_1)A_2^{(\text{Echo})}(\omega_2), \tag{56}$$

$$f_s^{(\text{Antiecho})}(t_1,\omega_2)=2a(-t_1)A_2^{(\text{Antiecho})}(\omega_2). \tag{57}$$

In other words, *applying the shearing transformation is equivalent to shifting the acquisition period from* t_2 *to* t_2' [Figs. 1(c) and 1(d)], that is, the ''acquisition'' of the time-domain signal starts at the position of the echo.

Two definitions of the evolution period appear in the literature. The first one, proposed by Medek *et al.*[32] and also applied by Hanaya and Harris,[45,54] considers the experimental or MQ coherence evolution period t_1 as the evolution period [Fig. 1(d)]. *This convention for the evolution period is call Cz in the remainder of the paper*. Thus, the original phase functions $a(t_1)$ and $a(-t_1)$ are unchanged, and the 2D spectra are simply

$$f_s^{(\text{Echo})}(\omega_1,\omega_2)=2A_2^{(\text{Echo})}(\omega_2)S_{1s}^{(\text{Echo})}(\omega_1), \tag{58}$$

$$f_s^{(\text{Antiecho})}(\omega_1,\omega_2)=2A_2^{(\text{Antiecho})}(\omega_2)S_{1s}^{(\text{Antiecho})}(\omega_1), \tag{59}$$

with

$$S_{1s}^{\text{Echo}}(\omega_1)=\int_0^{+\infty}a(t_1)\exp(-i\omega_1 t_1)dt_1, \tag{60}$$

$$S_{1s}^{(\text{Antiecho})}(\omega_1)=\int_0^{+\infty}a(-t_1)\exp(-i\omega_1 t_1)dt_1. \tag{61}$$

In contrast to Eqs. (52) and (53), Eqs. (58) and (59) show that the 2D spectra are products of two functions of independent variables. Equations (60) and (61) mean that a high-resolution spectrum appears along the F_1 dimension for $S_{1s}^{(\text{Echo})}(\omega_1)$ and $S_{1s}^{(\text{Antiecho})}(\omega_1)$, whose positions are $\omega_1=-\omega_{F_1}(I,p)$ and $\omega_1=\omega_{F_1}(I,p)$, respectively.

Equations (60) and (61) show that $S_{1s}^{(\text{Echo})}(\omega_1)$ and $S_{1s}^{(\text{Antiecho})}(\omega_1)$ are not pure absorption spectra. To achieve this, *we reverse the 2D spectrum of the antiecho signal* to change the direction of the F_1 dimension[76]

$$f_s^{(\text{Antiecho})}(-\omega_1,\omega_2)=A_2^{(\text{Antiecho})}(\omega_2)S_{1s}^{(\text{Antiecho})}(-\omega_1). \tag{62}$$

This transformation is equivalent to reversing the sign of t_1 in Eq. (61),

$$S_{1s}^{(\text{Antiecho})}(-\omega_1)=\int_{-\infty}^{0}a(t_1)\exp(-i\omega_1 t_1)dt_1. \tag{63}$$

Adding the 2D spectrum of the echo signal and the reversed 2D spectrum of the antiecho signal gives

$$\begin{aligned}f_s^{(\text{Echo})}(\omega_1,\omega_2)+f_s^{(\text{Antiecho})}(-\omega_1,\omega_2)&=2A_2^{(\text{Echo})}(\omega_2)S_{1s}^{(\text{Echo})}(\omega_1)\\&\quad+2A_2^{(\text{Antiecho})}(\omega_2)S_{1s}^{(\text{Antiecho})}(-\omega_1).\end{aligned} \tag{64}$$

If, furthermore, $A_2^{(\text{Echo})}(\omega_2)=A_2^{(\text{Antiecho})}(\omega_2)$, (However, this condition is not fulfilled in the two-pulse MQ-MAS sequence because only a part of the antiecho signal is acquired), then

$$\begin{aligned}f_s^{(\text{Echo})}(\omega_1,\omega_2)+f_s^{(\text{Antiecho})}(-\omega_1,\omega_2)&=2A_2^{(\text{Echo})}(\omega_2)[S_{1s}^{(\text{Echo})}(\omega_1)+S_{1s}^{(\text{Antiecho})}(-\omega_1)]\\&=2A_2^{(\text{Echo})}(\omega_2)\int_{-\infty}^{+\infty}a(t_1)\exp(-i\omega_1 t_1)dt_1\\&=2A_2^{(\text{Echo})}(\omega_2)\,\delta_D[\omega_1+\omega_{F_1}(I,p)].\end{aligned} \tag{65}$$

The Fourier transformation from minus infinity to plus infinity of the echo-phase function $a(t_1)$ *ensures that the resulting spectrum is a pure 2D absorption spectrum in the* F_1 *dimension.*[41,75,76,86] In our approximation, the spectrum along the F_1 dimension is the Dirac delta function δ_D. In other words, *a high-resolution spectrum is generated along the* F_1 *dimension.* The signal-to-noise ratio associated with the final 2D spectrum is larger than those of $f_s^{(\text{Echo})}(\omega_1,\omega_2)$ and $f_s^{(\text{Antiecho})}(\omega_1,\omega_2)$ [Eqs. (58) and (59)] by a factor of $\sqrt{2}$. Amoureux *et al.*[37] showed that only for a spin $I=\frac{3}{2}$ system it is possible to make the echo and antiecho amplitudes equal or to satisfy the condition $A_2^{(\text{Echo})}(\omega_2)=A_2^{(\text{Antiecho})}(\omega_2)$ by using suitable durations for the two rf pulses.

On the other hand, Massiot *et al.*[41] and Wang *et al.*[38] consider the position of the echo relative to the first rf pulse as the evolution period, which is described by $(1+k)t_1$ [Fig. 1(c)]. *In the remainder of the paper, this convention for the evolution period is called Ck*. Thus, the phases of the

echo and antiecho amplitudes become $a[(1+k)t_1]$ and $a[-(1+k)t_1]$ instead of $a(t_1)$ and $a(-t_1)$.[55] As a result, the 2D spectra are

$$f_s^{(\mathrm{Echo})}(\omega_1,\omega_2)=2A_2^{(\mathrm{Echo})}(\omega_2)\ \frac{1}{1+k}\ S_{1s}^{(\mathrm{Echo})}\left(\frac{\omega_1}{1+k}\right), \tag{66}$$

$$f_s^{(\mathrm{Antiecho})}(\omega_1,\omega_2)=2A_2^{(\mathrm{Antiecho})}(\omega_2)\ \frac{1}{1+k}\ S_{1s}^{(\mathrm{Antiecho})}\left(\frac{\omega_1}{1+k}\right). \tag{67}$$

Equations (66) and (67) are related to Eqs. (58) and (59) by the similarity theorem of the Fourier transformation.[1] The constant $1/(1+k)$, outside the functions, has no effect on the spectra. The arguments of $S_{1s}^{(\mathrm{Echo})}$ and $S_{1s}^{(\mathrm{Antiecho})}$ in Eqs. (58) and (59) concerning convention Cz are divided by $(1+k)$ in convention Ck. The new spectral width $\mathrm{SW1}_{Ck}$ is recalculated by replacing the increment of the experimental evolution period Δt_1 by $(1+k)\Delta t_1$, because we have the relation $\mathrm{SW1}_{Ck}\times(1+k)\Delta t_1=1$ for the simultaneous sampling method.[3] The well-known relation $2\mathrm{SW}\times\Delta t=1$ is for the sequential sampling method. The procedure described above [Eqs. (62)–(65)] to obtain a pure 2D absorption peak for convention Cz is valid for convention Ck and applicable to unsheared spectra.

The shearing transformation shifts the acquisition period from the end of the second rf pulse to the position of the echo. As a result, it separates the two parameters ω_1 and ω_2. A high-resolution isotropic spectrum is present along the F_1 dimension whereas a powder spectrum appears along the F_2 dimension. The 2D spectra resulting from the two conventions differ in the spectral width of the F_1 dimension. The spectral width associated with convention Ck is smaller than that associated with convention Cz by the factor $(1+k)$. Consequently, convention Ck produces a smaller linewidth in the F_1 dimension. *The scaling factor* $(1+k)$ *is the major drawback of convention* Ck. The linewidth depends on the value of k, which, for a given spin I, is associated with a coherence order p. In order to compare two linewidths along the F_1 dimension of two MQ-MAS spectra with different p, we have to multiply the linewidths by the scaling factor $(1+k)$ of each spectrum. That is, we return to convention Cz. In other words, *convention* Cz *makes linewidth comparison easier*. Similarly, convention Cz provides the experimental spinning rate along the F_1 dimension directly by measuring the difference in frequency separating two consecutive spinning sidebands,[45] whereas the spinning sidebands in convention Ck are scaled.[38] As will be shown in the next section, the choice of the evolution period has also an implication on the chemical shift labeling of the F_1 dimension of a sheared 2D spectrum, but it does not affect the chemical shift of the F_2 dimension.

At this point in data processing, we know how to shear 2D MQ-MAS data acquired with the hypercomplex method and to scale the high-resolution isotropic axis of the F_1 dimension in frequency units according to conventions Cz and Ck. In convention Cz, the dwell time in the F_1 dimension is the increment of the experimental evolution period. In convention Ck, the dwell time in the F_1 dimension is $(1+k)$ times the increment of the experimental evolution period.

F. Labeling the high-resolution isotropic axis in ppm

In a theoretical study, the chemical shifts of a peak along the F_1 and F_2 dimensions of a 2D spectrum are referenced to ω_0, which is located at the center of each of the two spectral widths. From a practical point of view, in a 1D spectrum or the F_2 dimension of a 2D spectrum, the chemical shift of an absorption line is referenced experimentally to an external aqueous solution with $\delta_{\mathrm{CS}}^{(\mathrm{iso})}=0$ ppm, by definition. For both dimensions of a 2D MQ-MAS spectrum, knowing the frequency offsets—Ω_{F_1} in the F_1 dimension and Ω_{F_2} in the F_2 dimension—of ω_0 relative to the aqueous solution allows us to express the observed chemical shifts of the center of gravity, $\delta_{G1}^{(\mathrm{obs})}$ in the F_1 dimension and $\delta_{G2}^{(\mathrm{obs})}$ in the F_2 dimension, of any peak relative to the aqueous solution. Unfortunately, Ω_{F_1} differs with Ω_{F_2} for an MQ-MAS spectrum. This section determines the relation between Ω_{F_1} and Ω_{F_2} for conventions Cz and Ck.

If the acquisition of the data starts at the position $t_2=kt_1$ of the echo—i.e., at the top of the echo—the position $\omega_{F_1}(I,p)$ of a peak relative to ω_0 along the F_1 dimension is given by Eq. (37). Therefore, the observed chemical shift of its center of gravity $\delta_{G1}^{(\mathrm{obs})}$ is equal to its position divided by ω_0:[87,88]

$$\delta_{G1}^{(\mathrm{obs})}=\omega_{F_1}(I,p)/\omega_0. \tag{68}$$

As the purpose of the shearing transformation is to shift the data acquisition from the end of the second rf pulse to the position or the top of the echo, Eq. (37) remains valid for a sheared 2D spectrum. Of course, it is meaningless to shear a 2D spectrum of a single crystal where a peak has no dispersion of orientation parameters. On the other hand, a powder sample presents dispersions due to the orientation distribution of all the crystallites. Shearing is necessary to obtain a high-resolution isotropic spectrum along the F_1 dimension. In the remainder of the paper 2D MQ-MAS spectra are always assumed to be sheared.

Along the F_1 dimension, the observed chemical shift of the center of gravity of a peak relative to ω_0, Eq. (68), using convention Cz is

$$\begin{aligned}\delta_{G1z}^{(\mathrm{obs})}&=(k-p)\,\delta_{\mathrm{CS}}^{(\mathrm{iso})}+(k+\lambda)\ \frac{\omega_{-1/2,1/2}^{(2)\mathrm{iso}}}{\omega_0}\\&=k_{1z}\delta_{\mathrm{CS}}^{(\mathrm{iso})}+k_{2z}\ \frac{\omega_{-1/2,1/2}^{(2)\mathrm{iso}}}{\omega_0}.\end{aligned} \tag{69}$$

That corresponding to convention Ck is

$$\delta_{G1k}^{(\mathrm{obs})}=\frac{1}{1+k}\ \delta_{G1z}^{(\mathrm{obs})}=k_{1k}\delta_{\mathrm{CS}}^{(\mathrm{iso})}+k_{2k}\ \frac{\omega_{-1/2,1/2}^{(2)\mathrm{iso}}}{\omega_0}. \tag{70}$$

The two observed chemical shifts $\delta_{G1k}^{(\mathrm{obs})}$ and $\delta_{G1z}^{(\mathrm{obs})}$ are related by the same factor as the spectral widths in conventions Ck and Cz. Table I shows that $k_{1z}=-1.7\ k_{2z}$ and $k_{1k}=-1.7\ k_{2k}$. Most of the values of k_{1k} in Table I differ with those given by Wang *et al.*;[38] on the other hand, we agree with all of the values of k_{2k}. Equation (69) is in agreement with that of Medek *et al.*[32] and of Hanaya and Harris[45] for $I=\frac{3}{2}$ and $p=-3$, except that their second-order quadrupole shift of

the center of gravity of the central line for $I=\frac{3}{2}$ is a factor of three smaller than that defined by Eq. (24). Equation (70) is also in agreement with that of Baltisberger *et al.*[40] for $I=\frac{5}{2}$ and $p=3$, and with that of Wu *et al.*[55] for $I=\frac{3}{2}$ and $p=-3$, except that the latter authors used a *negative* value for ω_0.

As the observed chemical shift of the center of gravity of a peak relative to ω_0 along the F_2 dimension is[12]

$$\delta_{G2}^{(\mathrm{obs})}=\delta_{\mathrm{CS}}^{(\mathrm{iso})}+\frac{\omega_{-1/2,1/2}^{(2)\mathrm{iso}}}{\omega_0}, \tag{71}$$

Eqs. (69) and (71) allow us to deduce the true isotropic chemical shift $\delta_{\mathrm{CS}}^{(\mathrm{iso})}$ of a peak relative to ω_0 for convention Cz:

$$\delta_{\mathrm{CS}}^{(\mathrm{iso})}=\frac{(k+\lambda)\,\delta_{G2}^{(\mathrm{obs})}-\delta_{G1z}^{(\mathrm{obs})}}{p+\lambda}=\frac{10}{27}\,\delta_{G2}^{(\mathrm{obs})}+k_{Gz}\delta_{G1z}^{(\mathrm{obs})}. \tag{72}$$

Similarly, Eqs. (70) and (71) allow us to deduce the true isotropic chemical shift of a peak relative to ω_0 for convention Ck:

$$\delta_{\mathrm{CS}}^{(\mathrm{iso})}=\frac{(k+\lambda)\,\delta_{G2}^{(\mathrm{obs})}-(1+k)\,\delta_{G1k}^{(\mathrm{obs})}}{p+\lambda}=\frac{10}{27}\,\delta_{G2}^{(\mathrm{obs})}+k_{Gk}\delta_{G1k}^{(\mathrm{obs})}. \tag{73}$$

The numerical values of k_{Gz} and k_{Gk} for the four half-integer quadrupole spins are reported in Table I. Of course, $\delta_{\mathrm{CS}}^{(\mathrm{iso})}$ itself is independent of conventions and depends only on the aqueous solution used as reference.

As mentioned above, the frequency offset Ω_{F_2} of ω_0 relative to the aqueous solution is used to establish the zero ppm position for the chemical shift scale along the F_2 dimension. It is not possible to set the zero ppm position in the F_1 dimension experimentally. We must compute the frequency offset Ω_{F_1} of ω_0 relative to the aqueous solution in the F_1 dimension. Since the Hamiltonian associated with a frequency offset and that of the isotropic chemical shift H_{CS} are similar, the expressions about the isotropic chemical shift, such as Eqs. (69) and (70), remain valid for the frequency offset. By analogy with Eqs. (69) and (70), where the second-order quadrupole shift of the center of gravity of the central line was deleted, because this contribution is meaningless for an aqueous solution, we deduce that

$$\Omega_{F_{1z}}=(k-p)\Omega_{F_2}=k_{1z}\Omega_{F_2} \tag{74}$$

for convention Cz and

$$\Omega_{F_{1k}}=\frac{1}{1+k}\,\Omega_{F_{1z}}=k_{1k}\Omega_{F_2} \tag{75}$$

for convention Ck. Equation (74) is in agreement with that of Hanaya and Harris[45] for $I=\frac{3}{2}$ and $p=-3$. Equation (75) is in agreement with that of Massiot.[46]

The zero ppm position of the chemical shift in the F_1 dimension is defined by the offset of ω_0 relative to the aqueous solution whose Larmor frequency is equal to $\omega_0/(2\pi)$ minus Ω_{F_1}:[3]

$$\frac{\Omega_{F_{1z}}}{\omega_0/(2\pi)-\Omega_{F_{1z}}}\approx\frac{\Omega_{F_{1z}}}{\omega_0/(2\pi)} \tag{76}$$

for convention Cz and

$$\frac{\Omega_{F_{1k}}}{\omega_0/(2\pi)-\Omega_{F_{1k}}}\approx\frac{\Omega_{F_{1k}}}{\omega_0/(2\pi)} \tag{77}$$

for convention Ck. As k_{1z} is larger than k_{1k}, the following relation must be satisfied:

$$\frac{\Omega_{F_{1z}}}{\omega_0/(2\pi)}=\frac{\Omega_{F_{1k}}}{\omega_0/(2\pi)}+(k_{1z}-k_{1k})\,\frac{\Omega_{F_2}}{\omega_0/(2\pi)}. \tag{78}$$

The approximation made in Eqs. (76) and (77) is applied in practice.[87,88] Now we know the position of an absorption line relative to ω_0 and the offset of ω_0 relative to the aqueous solution. Therefore we know the position of the absorption line relative to the aqueous solution, which is what we are looking for. *Equations (71), (72), and (73) remain valid even when the observed chemical shifts of the center of gravity of a peak along the two axes are referenced to an aqueous solution instead of* ω_0.

We also deduce the second-order quadrupole shift of the center of the gravity of a peak

$$\begin{aligned}\frac{\omega_{-1/2,1/2}^{(2)\mathrm{iso}}}{\omega_0}&=\frac{1}{\lambda+p}\,[\,\delta_{G1z}^{(\mathrm{obs})}-(k-p)\,\delta_{G2}^{(\mathrm{obs})}]\\&=-k_{Gz}[\,\delta_{G1z}^{(\mathrm{obs})}-k_{1z}\delta_{G2}^{(\mathrm{obs})}]\end{aligned} \tag{79}$$

for convention Cz using Eqs. (69) and (71), and

$$\begin{aligned}\frac{\omega_{-1/2,1/2}^{(2)\mathrm{iso}}}{\omega_0}&=\frac{1+k}{\lambda+p}\left[\,\delta_{G1k}^{(\mathrm{obs})}-\frac{k-p}{1+k}\,\delta_{G2}^{(\mathrm{obs})}\right]\\&=-k_{Gk}[\,\delta_{G1k}^{(\mathrm{obs})}-k_{1k}\delta_{G2}^{(\mathrm{obs})}]\end{aligned} \tag{80}$$

for convention Ck using Eqs. (70) and (71). However, Eqs. (79) and (80) do not allow us to determine the quadrupole coupling constant and the asymmetry parameter η independently. The latter may be obtained by fitting the line shape of the cross-section (parallel to the F_2 dimension) of the peak. If the spectrum has a featureless line shape, the parameter $C_{Q\eta}$ defined by Eq. (26c) is commonly used for characterizing a material:

$$\begin{aligned}C_{Q\eta}=I(2I-1)\,\frac{\omega_0}{2\pi}\,\sqrt{\frac{40}{3[I(I+1)-\frac{3}{4}]}}\\\times\sqrt{k_{Gz}[\,\delta_{G1z}^{(\mathrm{obs})}-k_{1z}\delta_{G2}^{(\mathrm{obs})}]}\end{aligned} \tag{81}$$

for convention Cz and

$$\begin{aligned}C_{Q\eta}=I(2I-1)\,\frac{\omega_0}{2\pi}\,\sqrt{\frac{40}{3[I(I+1)-\frac{3}{4}]}}\\\times\sqrt{k_{Gk}[\,\delta_{G1k}^{(\mathrm{obs})}-k_{1k}\delta_{G2}^{(\mathrm{obs})}]}\end{aligned} \tag{82}$$

for convention Ck.

As for $\delta_{\mathrm{CS}}^{(\mathrm{iso})}$, the numerical value of $\omega_{-1/2,1/2}^{(2)\mathrm{iso}}$ and $C_{Q\eta}$ are independent of conventions. They are related to two experi-

mental values, the observed chemical shifts of the center of gravity of a peak in the F_1 and F_2 dimensions. Fernandez *et al.*[67] established similar but not identical expressions of $\delta_{CS}^{(iso)}$ for unsheared and sheared spectra.

To summarize, the choice of the convention modifies not only the spectral width or the chemical shift range along the F_1 dimension (see Sec. II E) but also the observed chemical shift of the center of gravity of a peak relative to an external aqueous solution. However, the true isotropic chemical shift $\delta_{CS}^{(iso)}$ still allows us to compare the experimental results from different authors. Fortunately, the F_2 dimension does not depend on the conventions, but the powder line shape may be distorted by the MQ effects.

At this stage in data processing, we know how to use Eqs. (74) or (75) to define the zero ppm position of the high-resolution isotropic axis in the F_1 dimension. The observed chemical shifts of the center of gravity of a peak in both dimensions are referenced to the aqueous solution instead of to ω_0, thanks to Eqs. (74) or (75). The true isotropic chemical shift is provided by Eqs. (72) or (73), and the parameter $C_{Q\eta}$ by Eqs. (81) or (82), according to conventions Cz or Ck.

III. EXPERIMENT

The sample was rubidium nitrate $RbNO_3$ powder. The ^{87}Rb ($I=\frac{3}{2}$) 2D 3Q-MAS spectra were obtained on Bruker multinuclear spectrometers ASX-300 and -500 operating at 98.2 and 163.6 MHz, respectively. Standard high power MAS probeheads equipped with 4 mm diameter rotors were used. The rotor spinning rate was 10 kHz. The two-pulse 3Q-MAS acquisition program with hypercomplex procedure was kindly provided by Massiot. The chemical shift was referenced to an external aqueous solution of 1 M of $RbNO_3$ which was used to determine the amplitude ω_{rf} of the rf pulse. The experiments were carried out on-resonance with a recycle delay of 1 s.

At 98.2 MHz, $\omega_{rf}/(2\pi)=83.3$ kHz, corresponding to a $\pi/2$ pulse duration of 3 μs. The first- and second-pulse durations were 7 and 2 μs, respectively. The offset of the carrier frequency relative to the aqueous solution is $\Omega_{F_2}=-3535$ Hz. At 163.6 MHz, $\omega_{rf}/(2\pi)=100$ kHz, corresponding to a $\pi/2$ pulse duration of 2.5 μs. The first- and second-pulse durations were 4.5 and 4 μs, respectively. The offset of the carrier frequency was $\Omega_{F_2}=-4786$ Hz.

The acquisition of the two t_2-domain signals in quadrature was performed in simultaneous mode[89,90] like the hypercomplex or States *et al.* method. The dwell time was 50 μs, corresponding to a spectral width in the F_2 dimension of 20 kHz. The acquisition for 256 complex data points was 12.8 ms. There were 128 increments of the experimental evolution period in steps of 30 μs.

The data processing program including the shearing transformation, written for Macintosh computers, was downloaded from the WEB page of Grandinetti.[91] Zero filling was performed twice for the F_1 dimension. In this dimension, the dwell time for convention Cz is 30 μs and 53.33 μs$=(1+k)\times 30$ μs for convention Ck. The offset of the carrier frequency relative to the aqueous solution in the F_1 dimension is $\Omega_{F_{1z}}$, equal to $k_{1z}(=34/9)$ times Ω_{F_2}, for convention Cz. For convention Ck, $\Omega_{F_{1k}}$ was equal to $k_{1k}(=17/8)$ times Ω_{F_2}.

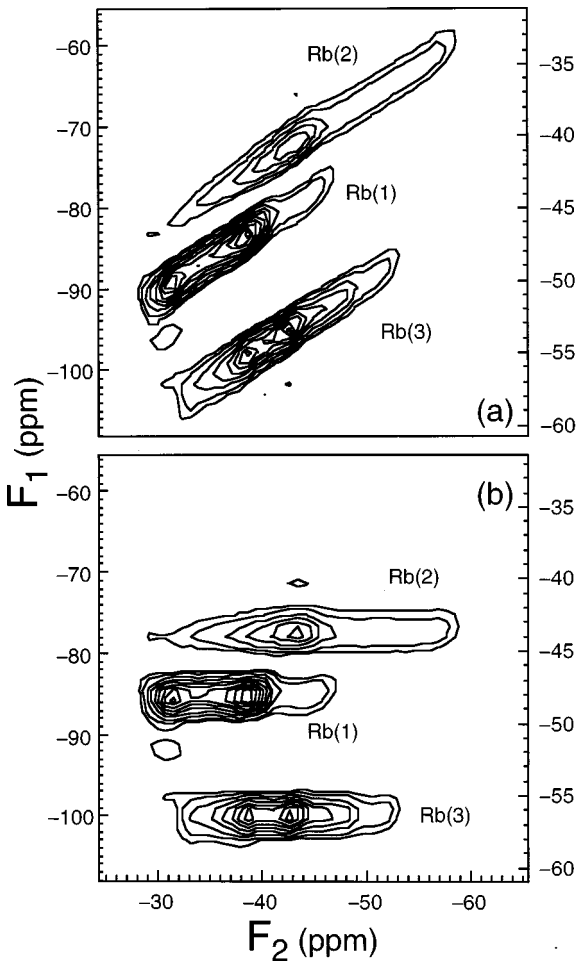

FIG. 4. Contour plot of the unsheared (a) and sheared (b) 2D 3Q-MAS spectra of the ^{87}Rb ($I=\frac{3}{2}$) nuclei in $RbNO_3$ powder, obtained at 98.2 MHz. The three ^{87}Rb sites, Rb(1), Rb(2), and Rb(3), are observed. Their contour lines are drawn every 10% starting at a level of 7% and ending at 97% of the maximum point in the spectrum. The left-hand side axis is labeled with convention Cz and the right-hand side axis with convention Ck.

IV. RESULTS

Figure 4 shows the contour plots of the unsheared and sheared 2D 3Q-MAS spectra of ^{87}Rb acquired at 98.2 MHz. The left-hand axis is labeled according to convention Cz whereas the right-hand axis is for convention Ck. Scaling and labeling the F_1 dimension are independent of the shearing transformation. However, a sheared 2D spectrum makes the interpretation simpler. The linewidths of the three rubidium sites in the F_2 dimension, Rb(1), Rb(2), and Rb(3), are different, ranging from 20 to 30 ppm, and are independent of the shearing transformation. On the other hand, the linewidths of the three sites along the F_1 dimension in the sheared spectrum [Fig. 4(b)] are similar and much smaller than those of the three sites along the F_2 dimension, less than 8 ppm for convention Cz and less than 4 ppm for convention Ck.

Figure 5(a) presents the cross-section spectra [parallel to

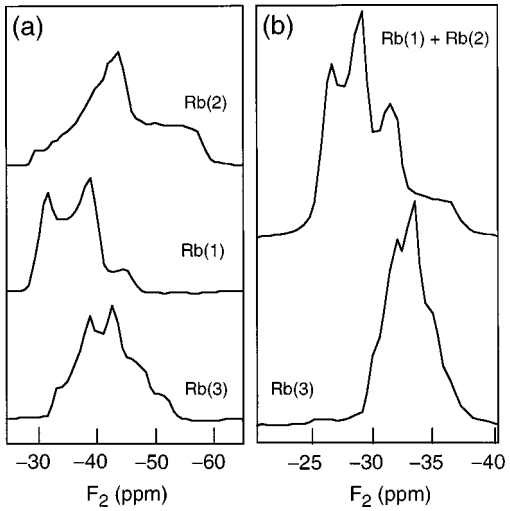

FIG. 5. Cross-section spectra (parallel to the F_2 dimension) of the sheared 2D 3Q-MAS spectrum of the ^{87}Rb ($I=\frac{3}{2}$) nuclei in $RbNO_3$ powder, obtained at (a) 98.2 MHz [Fig. 4(b)] and (b) at 163.6 MHz (Fig. 6). The three chemical shift data for each ^{87}Rb site are given in the following order: first the observed chemical shift of the center of gravity $\delta_{G2}^{(\mathrm{obs})}$ of a peak along the F_2 dimension, then the observed chemical shifts $\delta_{G1z}^{(\mathrm{obs})}$ and $\delta_{G1k}^{(\mathrm{obs})}$, along the F_1 dimension, of the cross section for conventions Cz and Ck. In (a), (-35.2, -85.6, and -48.1 ppm) for Rb(1), (-42.4, -77.6, and -43.7 ppm) for Rb(2), and (-40.8, -100.2, and -56.3 ppm) for Rb(3). In (b), (nd, -87.4, and -49.2 ppm) for Rb(1)+Rb(2) and (-32.2, -103.3, and -58.1 ppm) for Rb(3).

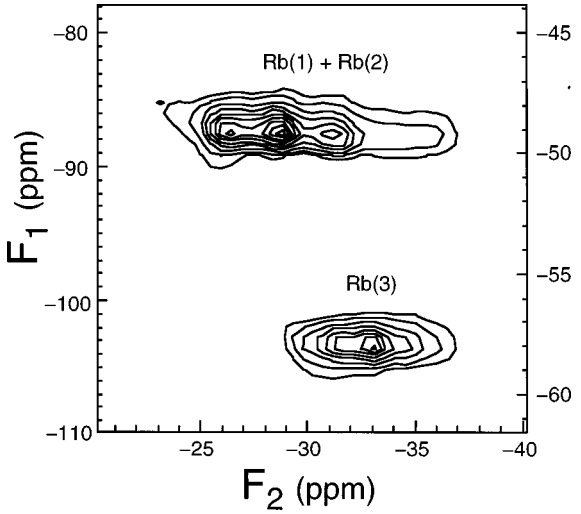

FIG. 6. Contour plot of the sheared 2D 3Q-MAS spectrum of the ^{87}Rb ($I=\frac{3}{2}$) nuclei in $RbNO_3$ powder, obtained at 163.6 MHz. Two of the three ^{87}Rb sites, Rb(1) and Rb(2) observed in Fig. 4, are not resolved. Their contour lines are drawn every 10% starting at a level of 7% and ending at 97% of the maximum point in the spectrum. The left-hand side axis is labeled with convention Cz and the right-hand side axis with convention Ck.

the F_2 dimension in Fig. 4(b)] of the three sites. The chemical shifts along the F_1 dimension of these cross-section spectra are considered as the observed chemical shifts of the center of gravity of the spectrum along the F_1 dimension. Their values, $\delta_{G1z}^{(\mathrm{obs})}$ for convention Cz and $\delta_{G1k}^{(\mathrm{obs})}$ for convention Ck, are reported in Table III. The observed chemical shifts of the center of gravity along the F_2 dimension $\delta_{G2}^{(\mathrm{obs})}$ of these three cross-section spectra, reported in Table III are determined by the point at which the integral of the spectrum is half that of the full spectrum. The true isotropic chemical shifts of these three sites, deduced from the observed chemical shifts in both dimensions using Eqs. (72) or (73), are reported in Table III. They are similar to those of Massiot *et al.*[41] and of Hanaya and Harris.[45]

The three line shapes in Fig. 5(a) are similar to those of Massiot *et al.*[41] and of Hanaya and Harris,[45] who used simulated spectra to determine the quadrupole coupling constant and the asymmetry parameter of each site. The parameters $C_{Q\eta}=(e^2qQ/h)(\eta^2/3+1)^{1/2}$ of the three sites, deduced from their results, are reported in Table III. We have also reported our own values of $C_{Q\eta}$ obtained from the two observed chemical shifts of the center of gravity of each site using Eqs. (81) or (82). Our values for Rb(1) and Rb(2) are very close to those of Massiot *et al.*[41] and of Hanaya and Harris.[45] Only that of Rb(3) differs a little.

Figure 6 displays the contour plot of the sheared 2D 3Q-MAS spectrum of ^{87}Rb acquired at 163.6 MHz; the axes are labeled as in Fig. 4. The Rb(1) and Rb(2) sites are not resolved as observed by Wang *et al.*,[38] who worked with the same Larmor frequency. This is not surprising, since at 130.9 MHz these two sites are hardly resolved.[51,78] Due to a higher Larmor frequency, which makes the second-order quadrupole interaction weaker, the linewidths expressed in ppm along the F_2 dimension are much smaller than those in Fig. 4(b). When the linewidths are expressed in frequency units, the ratio of the linewidths is inversely proportional to the ratio of the Larmor frequencies. On the other hand, the line-

TABLE III. Various parameters of the three rubidium ^{87}Rb ($I=\frac{3}{2}$) sites in $RbNO_3$ powder deduced from sheared 2D 3Q-MAS spectra: $\delta_{G2}^{(\mathrm{obs})}$ is the observed chemical shift of the center of gravity of a peak along the F_2 dimension, $\delta_{G1z}^{(\mathrm{obs})}$ and $\delta_{G1k}^{(\mathrm{obs})}$ are, respectively, the observed chemical shifts of the center of gravity of a peak along the F_1 dimension according to conventions Cz and Ck, and $\delta_{\mathrm{CS}}^{(\mathrm{iso})}$ is the true isotropic chemical shift of a peak. Chemical shifts are expressed in ppm and $C_{Q\eta}=(e^2qQ/h)(\eta^2/3+1)^{1/2}$ in MHz units.

	This work										Massiot *et al.* (Ref. 41)			Hanaya and Harris (Ref. 45)	
	163.6 MHz					98.2 MHz					98.2 MHz			65.5 MHz	
Site	$\delta_{G2}^{(\mathrm{obs})}$	$\delta_{G1z}^{(\mathrm{obs})}$	$\delta_{G1k}^{(\mathrm{obs})}$	$\delta_{\mathrm{CS}}^{(\mathrm{iso})}$	$C_{Q\eta}$	$\delta_{G2}^{(\mathrm{obs})}$	$\delta_{G1z}^{(\mathrm{obs})}$	$\delta_{G1k}^{(\mathrm{obs})}$	$\delta_{\mathrm{CS}}^{(\mathrm{iso})}$	$C_{Q\eta}$	$\delta_{G1k}^{(\mathrm{obs})}$	$\delta_{\mathrm{CS}}^{(\mathrm{iso})}$	$C_{Q\eta}$	$\delta_{\mathrm{CS}}^{(\mathrm{iso})}$	$C_{Q\eta}$
Rb(1)	nd	-87.4	-49.2	nd	nd	-35.2	-85.6	-48.1	**-27.3**	**1.74**	-49.0	**-27.4**	**1.69**	**-27.5**	**1.71**
Rb(2)	nd	-87.4	-49.2	nd	nd	-42.4	-77.6	-43.7	**-28.6**	**2.30**	-44.7	**-28.5**	**2.24**	**-28.9**	**2.29**
Rb(3)	-32.2	-103.3	-58.1	**-29.1**	**1.81**	-40.8	-100.2	-56.3	**-31.8**	**1.86**	-57.1	**-31.3**	**1.79**	**-31.4**	**1.79**

widths expressed in ppm along the F_1 dimension are comparable to those in Fig. 4(b). This suggests that the linewidth in the F_1 dimension is dominated by the anisotropy of the chemical shift.

The line shape of the Rb(1)+Rb(2) in Fig. 5(b) is nearly the sum of those in Fig. 5(a). The observed chemical shifts are reported in Table III. Only the data concerning Rb(3) are analyzed. Its true isotropic chemical shift is smaller than that determined at 98.2 MHz but the parameter $C_{Q\eta}$ has a value similar to that of Massiot *et al.*[41] and those of Hanaya and Harris.[45] Simulation of Rb(1)+Rb(2) spectrum in Fig. 5(b) should yield the observed chemical shift of the center of gravity $\delta_{G2}^{(\mathrm{obs})}$ of these two sites.

V. CONCLUSIONS

We have analyzed the successive stages of a two-pulse MQ-MAS experiment with the hypercomplex detection method in order to scale in frequency units and to label in chemical shift units the high-resolution isotropic axis of the F_1 dimension, taking into account conventions Cz and Ck. Convention Cz is preferable to convention Ck, because the latter introduces the scaling factor $(1+k)$, modifying not only the spectral width and the linewidth, but also the positions of the spinning sidebands along the F_1 dimension. Sheared 2D spectra allow us to determine the true isotropic chemical shift, the second-order quadrupole shift of the center of gravity of a peak, and the parameter $C_{Q\eta}$. The latter is of importance for characterizing featureless line shapes in the F_2 dimension. Experimental verifications on the rubidium nuclei in $RbNO_3$ show that experiments should still be carried out with several magnetic fields $\mathbf{B}_0$ in order to resolve all the peaks in the F_1 dimension. The validity of the analytical expressions concerning the true isotropic chemical shift, the second-order quadrupole shift of the center of gravity of a peak, and the parameter $C_{Q\eta}$ should be checked for other MQ-MAS sequences such as the z-filter sequence.

ACKNOWLEDGMENTS

We thank Dr. Massiot for providing the two-pulse 3Q-MAS acquisition program with the hypercomplex detection method, Professor Grandinetti for his processing program RMN (FAT) allowing the shearing transformation, and C. Gervais (Laboratoire de Chimie de la Matière Condensée, CNRS URA 1466) for her help with RMN (FAT).

[1] R. R. Ernst, G. Bodenhausen, and A. Wokaun, *Principles of Nuclear Magnetic Resonance in One and Two Dimensions* (Clarendon, Oxford, 1990).
[2] R. Freeman, *Spin Choreography, Basic Steps in High Resolution NMR* (Spektrum Academic, Oxford, 1997).
[3] F. J. M. Van de Ven, *Multidimensional NMR in Liquids, Basics Principles and Experimental Methods* (VCH, New York, 1995).
[4] M. Goldman, *Quantum Description of High-Resolution NMR in Liquids* (Clarendon, Oxford, 1988).
[5] K. Schmidt-Rohr and H. W. Spiess, *Multidimensional Solid-State NMR and Polymers* (Academic, San Diego, 1994).
[6] J. Haase and E. Oldfield, J. Magn. Reson., Ser. A **101**, 30 (1993).
[7] J. Haase and E. Oldfield, J. Magn. Reson., Ser. A **104**, 1 (1993).
[8] D. Freude and J. Haase, in *NMR Basic Principles and Progress*, edited by P. Diehl, E. Fluck, H. Günter, R. Kosfeld, and J. Seelig (Springer-Verlag, Berlin, 1993), Vol. 29.
[9] S. Vega and Y. Naor, J. Chem. Phys. **75**, 75 (1981).
[10] A. Abragam, *The Principles of Nuclear Magnetism* (Clarendon, Oxford, 1961).
[11] D. Massiot (unpublished).
[12] P. P. Man, Phys. Rev. B **55**, 8406 (1997).
[13] P. P. Man, in *Encyclopedia of Nuclear Magnetic Resonance*, edited by D. M. Grant and R. K. Harris (Wiley, Chichester, 1996), p. 3838.
[14] E. K. Jang and O. H. Han, J. Korean Phys. Soc. **30**, 115 (1997).
[15] A. Samoson, E. Kundla, and E. Lippmaa, J. Magn. Reson. **49**, 350 (1982).
[16] A. P. M. Kentgens, J. J. M. Lemmens, F. M. M. Geurts, and W. S. Veeman, J. Magn. Reson. **71**, 62 (1987).
[17] P. P. Man, H. Theveneau, and P. Papon, J. Magn. Reson. **64**, 271 (1985).
[18] S. Ding and C. A. McDowell, J. Magn. Reson., Ser. A **112**, 36 (1995).
[19] A. Samoson and E. Lippmaa, J. Magn. Reson. **79**, 255 (1988).
[20] P. P. Man, Mol. Phys. **78**, 307 (1993).
[21] P. P. Man and P. Tougne, Mol. Phys. **83**, 997 (1994).
[22] R. Janssen, G. A. H. Tijink, and W. S. Veemann, J. Chem. Phys. **88**, 518 (1988).
[23] G. A. H. Tijink, R. Janssen, and W. S. Veeman, J. Am. Chem. Soc. **109**, 7301 (1987).
[24] A. P. M. Kentgens, J. Magn. Reson., Ser. A **104**, 302 (1993).
[25] H. Kraus, R. Prins, and A. P. M. Kentgens, J. Phys. Chem. **100**, 16 336 (1996).
[26] J. Haase, D. Freude, H. Pfeifer, E. Lippmaa, and P. Sarv, Chem. Phys. Lett. **152**, 254 (1988).
[27] J. Haase and H. Pfeifer, J. Magn. Reson. **86**, 217 (1990).
[28] P. J. Grandinetti, in *Encyclopedia of Nuclear Magnetic Resonance* (Ref. 13), p. 1768.
[29] J. S. Shore, S. H. Wang, R. E. Taylor, A. T. Bell, and A. Pines, J. Chem. Phys. **105**, 9412 (1996).
[30] A. Medek, J. R. Sachleben, P. Beverwyk, and L. Frydman, J. Chem. Phys. **104**, 5374 (1996).
[31] L. Frydman and J. S. Harwood, J. Am. Chem. Soc. **117**, 5367 (1995).
[32] A. Medek, J. S. Harwood, and L. Frydman, J. Am. Chem. Soc. **117**, 12 779 (1995).
[33] R. Tycko, in *Encyclopedia of Nuclear Magnetic Resonance* (Ref. 13), p. 3425.
[34] A. Wokaun and R. R. Ernst, Chem. Phys. Lett. **52**, 407 (1977).
[35] P. P. Man, Phys. Rev. B **52**, 9418 (1995).
[36] P. P. Man, J. Chem. Phys. **106**, 3908 (1997).
[37] J.-P. Amoureux, C. Fernandez, and L. Frydman, Chem. Phys. Lett. **259**, 347 (1996).
[38] S. H. Wang, Z. Xu, J. H. Baltisberger, L. M. Bull, J. F. Stebbins, and A. Pines, Solid State Nucl. Magn. Reson. **8**, 1 (1997).
[39] L. Marinelli and L. Frydman, Chem. Phys. Lett. **275**, 188 (1997).
[40] J. H. Baltisberger, Z. Xu, J. F. Stebbins, S. H. Wang, and A. Pines, J. Am. Chem. Soc. **118**, 7209 (1996).

[41] D. Massiot, B. Touzo, D. Trumeau, J. P. Coutures, J. Virlet, P. Florian, and P. J. Grandinetti, Solid State Nucl. Magn. Reson. **6**, 73 (1996).
[42] S. P. Brown, S. J. Heyes, and S. Wimperis, J. Magn. Reson., Ser. A **119**, 280 (1996).
[43] S. P. Brown and S. Wimperis, J. Magn. Reson. **124**, 279 (1997).
[44] J.-P. Amoureux, C. Fernandez, and S. Steuernagel, J. Magn. Reson., Ser. A **123**, 116 (1996).
[45] M. Hanaya and R. K. Harris, J. Phys. Chem. A **101**, 6903 (1997).
[46] D. Massiot, J. Magn. Reson., Ser. A **122**, 240 (1996).
[47] M. J. Duer and C. Stourton, J. Magn. Reson. **124**, 189 (1997).
[48] T. Vosegaard, F. H. Larsen, H. J. Jakobsen, P. D. Ellis, and N. C. Nielsen, J. Am. Chem. Soc. **119**, 9055 (1997).
[49] G. Wu, D. Rovnyak, and R. G. Griffin, J. Am. Chem. Soc. **118**, 9326 (1996).
[50] M. J. Duer, Chem. Phys. Lett. **277**, 167 (1997).
[51] S. P. Brown and S. Wimperis, J. Magn. Reson. **128**, 42 (1997).
[52] A. Samoson, J. Magn. Reson., Ser. A **121**, 209 (1996).
[53] S. Ding and C. A. McDowell, Chem. Phys. Lett. **270**, 81 (1997).
[54] M. Hanaya and R. K. Harris, Solid State Nucl. Magn. Reson. **8**, 147 (1997).
[55] G. Wu, D. Rovnyak, B. Q. Sun, and R. G. Griffin, Chem. Phys. Lett. **249**, 210 (1996).
[56] M. Pruski, D. P. Lang, C. Fernandez, and J.-P. Amoureux, Solid State Nucl. Magn. Reson. **7**, 327 (1997).
[57] C. Fernandez, L. Delevoye, J.-P. Amoureux, D. P. Lang, and M. Pruski, J. Am. Chem. Soc. **119**, 6858 (1997).
[58] S. H. Wang, S. M. De Paul, and L. M. Bull, J. Magn. Reson. **125**, 364 (1997).
[59] S.-J. Hwang, C. Fernandez, J.-P. Amoureux, J. Cho, S. W. Martin, and M. Pruski, Solid State Nucl. Magn. Reson. **8**, 109 (1997).
[60] C. Fernandez and J.-P. Amoureux, Solid State Nucl. Magn. Reson. **5**, 315 (1996).
[61] L. Delevoye, S. X. Liu, M. D. Welch, C. Fernandez, J.-P. Amoureux, and J. Klinowski, J. Chem. Soc., Faraday Trans. **93**, 2591 (1997).
[62] A. Samoson, Chem. Phys. Lett. **247**, 203 (1995).
[63] J. V. Hanna, M. E. Smith, and H. J. Whitfield, J. Am. Chem. Soc. **118**, 5772 (1996).
[64] D. Massiot, R. Conanec, W. Feldmann, R. Marchand, and Y. Laurent, Inorg. Chem. **35**, 4957 (1996).
[65] C. Fernandez, J.-P. Amoureux, J. M. Chezeau, L. Delmotte, and H. Kessler, Microporous Mater. **6**, 331 (1996).
[66] C. Fernandez and J.-P. Amoureux, Chem. Phys. Lett. **242**, 449 (1995).
[67] C. Fernandez, J.-P. Amoureux, L. Delmotte, and H. Kessler, Microporous Mater. **6**, 125 (1996).
[68] J. Rocha, A. P. Esculcas, C. Fernandez, and J.-P. Amoureux, J. Phys. Chem. **100**, 17 889 (1996).
[69] P. Sarv, C. Fernandez, J.-P. Amoureux, and K. Keskinen, J. Phys. Chem. **100**, 19 223 (1996).
[70] J. Rocha, J. P. Lourenço, M. F. Ribeiro, C. Fernandez, and J.-P. Amoureux, Zeolites **19**, 156 (1997).
[71] J. Rocha, Z. Lin, C. Fernandez, and J.-P. Amoureux, J. Chem. Soc. Chem. Commun. 2513 (1996).
[72] P. J. Dirken, S. C. Kohn, M. E. Smith, and E. R. H. van Eck, Chem. Phys. Lett. **266**, 568 (1997).
[73] G. Wu, D. Rovnyak, P. C. Huang, and R. G. Griffin, Chem. Phys. Lett. **277**, 79 (1997).
[74] E. Lippmaa, A. Samoson, and M. Mägi, J. Am. Chem. Soc. **108**, 1730 (1986).
[75] P. J. Grandinetti, J. H. Baltisberger, A. Llor, Y. K. Lee, U. Werner, M. A. Eastman, and A. Pines, J. Magn. Reson., Ser. A **103**, 72 (1993).
[76] P. J. Grandinetti (unpublished).
[77] D. J. States, R. A. Haberkorn, and D. J. Ruben, J. Magn. Reson. **48**, 286 (1982).
[78] C. Fernandez and J.-P. Amoureux, Solid State Nucl. Magn. Reson. **5**, 315 (1996).
[79] C. P. Slichter, *Principles of Magnetic Resonance* (Springer-Verlag, Berlin, 1990).
[80] R. Kimmich, *NMR: Tomography, Diffusometry, Relaxometry* (Springer-Verlag, Berlin, 1997).
[81] S. Z. Ageev, P. P. Man, and B. C. Sanctuary, J. Magn. Reson. **128**, 12 (1997).
[82] J.-P. Amoureux, Solid State Nucl. Magn. Reson. **2**, 83 (1993).
[83] K. Nagayama, A. Kumar, K. Wüthrich, and R. R. Ernst, J. Magn. Reson. **40**, 321 (1980).
[84] P. J. Grandinetti, Y. K. Lee, J. H. Baltisberger, B. Q. Sun, and A. Pines, J. Magn. Reson., Ser. A **102**, 195 (1993).
[85] D. Massiot, I. Farnan, N. Gauthier, D. Trumeau, A. Trokiner, and J.-P. Coutures, Solid State Nucl. Magn. Reson. **4**, 241 (1995).
[86] J. Keller and D. Neuhaus, J. Magn. Reson. **63**, 454 (1985).
[87] R. K. Harris, *Nuclear Magnetic Resonance Spectroscopy* (Longman Scientific & Technical, Essex, 1987).
[88] H. Friebolin, *Basic One- and Two-Dimensional NMR Spectroscopy*, 2nd ed. (VCH, New York, 1993).
[89] A. E. Derome and M. P. Williamson, J. Magn. Reson. **88**, 177 (1990).
[90] C. J. Turner and H. D. W. Hill, J. Magn. Reson. **66**, 410 (1986).
[91] P. J. Grandinetti, RMN program, 1996, Department of Chemistry, Ohio State University, Colombus, Ohio.